Weierstraß-Institut
für Angewandte Analysis und Stochastik

Leibniz-Institut im Forschungsverbund Berlin e. V.

Preprint ISSN 2198-5855

Efficient numerical framework for geothermal energy production optimization in fracture-controlled reservoirs

Ondřej Pártl[1], Ernesto Meneses Rioseco[2]

submitted: January 21, 2025

[1] Weierstrass Institute
Mohrenstr. 39
10117 Berlin, Germany
E-Mail: ondrej.partl@wias-berlin.de

[2] Georg-August-Universität Göttingen
Dept. Structural Geology and Geothermics
Goldschmidtstr. 3
37077 Göttingen, Germany

LIAG-Institute for Applied Geophysics
Dept. Static Modeling
Stilleweg 2
30655 Hannover, Germany
E-Mail: ernesto.menesesrioseco@uni-goettingen.de

No. 3169
Berlin 2025

2020 *Mathematics Subject Classification.* 65M60, 76D55, 76S05.

Key words and phrases. Discrete fracture network, Porous medium, Fluid flow, Heat transport, Production optimization, Geothermal reservoir.

Edited by
Weierstraß-Institut für Angewandte Analysis und Stochastik (WIAS)
Leibniz-Institut im Forschungsverbund Berlin e. V.
Mohrenstraße 39
10117 Berlin
Germany

Fax: +49 30 20372-303
E-Mail: preprint@wias-berlin.de
World Wide Web: http://www.wias-berlin.de/

Efficient numerical framework for geothermal energy production optimization in fracture-controlled reservoirs

Ondřej Pártl, Ernesto Meneses Rioseco

1 Abstract

We describe an open-source numerical framework for the automated search for the placements of injection and production wells in hot fracture-controlled reservoirs that sustainably optimize geothermal energy production, where we consider deviated multiwell layouts (smart multiwell arrangement). This search is carried out via 3D simulations of groundwater flow and heat transfer. We model the reservoirs as discrete fracture networks (DFN) in which the fractures are 2D manifolds with polygonal boundaries embedded in a 3D porous medium. The wells are modeled via the immersed boundary method. The flow and heat transport in the DFN-matrix system are modeled by solving the balance equations for mass, momentum, and energy. The fully developed numerical framework combines the finite element method with semi-implicit time-stepping, algebraic flux correction, and approximation of the wells via the non-matching approach. To perform the optimization, we use various gradient-free algorithms. We present the results of verification and validation tests with DFNs of simple structure and realistic physical parameter values.

10.20347/WIAS.PREPRINT.3169 Berlin 2025

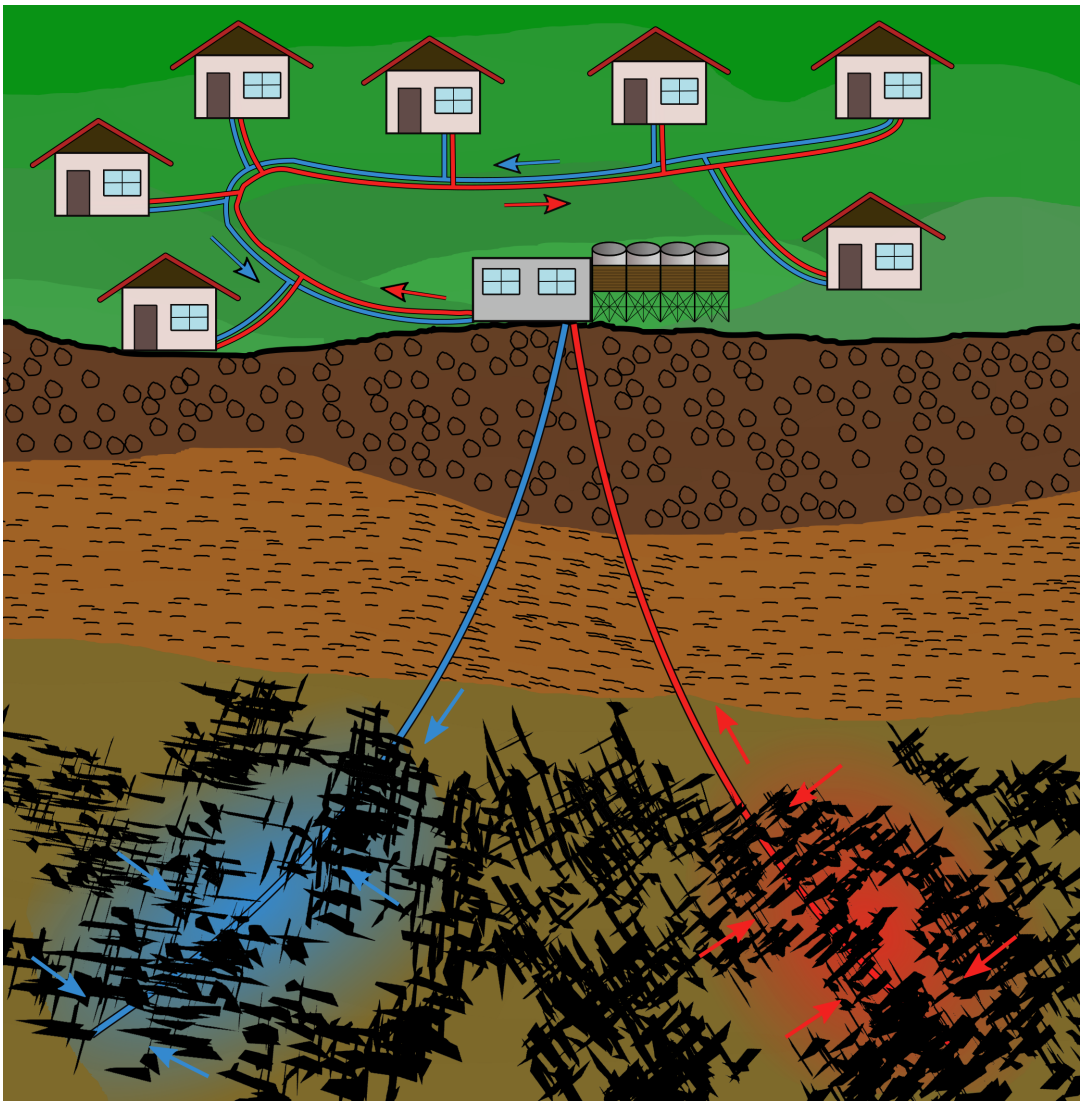

Figure 1: Schematic representation of a geothermal doublet concept targeting a fracture-controlled geothermal reservoir. A geothermal doublet is composed of an injection (blue) and a production (red) well. Heat is extracted from the produced reservoir fluid at the surface and injected at a lower temperature back into the reservoir.

2 Introduction

Decarbonizing the energy sector in Germany involves the development of diverse low-carbon technologies and renewable energy resources in an optimal and sustainable way [20, 26]. Among the different kinds of renewable energies, the use of deep geothermal resources has gained remarkable momentum in recent years due to its independence from climatic variability, its baseload availability and direct-use applications, as well as small land footprint, which makes these resources especially beneficial in highly urbanized or environmentally sensitive regions [12, 22]. In particular, the Greater Munich region in Germany shows one of the most dynamic developments in the use of deep geothermal resources in middle Europe [2, 25]. Numerous geothermal plants for district heating and electricity production have been put into operation during the last decades to meet the heat demand of several large villages in the surroundings of Munich. For illustration, see Figure 1.

With the increasing number of neighboring geothermal wells, questions related to the optimal placement of future wells and reservoir management in a sustainable way become more and more important. These questions are intimately linked to the kind of geothermal reservoir targeted. In particular, in sedimentary reservoir types [24], the permeability structure and type of flow regime are among the key factors in well placement optimization and

sustainable geothermal reservoir management [7]. The successful development of deep geothermal resources in the Greater Munich region is due to favorable hydrogeological and geothermal conditions encountered in porous, fractured, and karstified Upper Jurassic carbonates at varying depths [9].

Some works that address the hydraulic behavior of the Upper Jurassic reservoir suggest that despite its heterogeneity, it can be modeled using the equivalent porous medium (EPM) approach due to its generally observed radial flow regime [5, 6]. Other studies, however, indicate that fractured and faulted sectors of this geothermal reservoir exhibit a linear or bilinear flow regime, highlighting the hydraulic activity of fracture- or fault-controlled domains of the reservoir and the hydraulic interaction of the fracture-matrix system [29]. Most recently, a comprehensive study on a premature thermal breakthrough that occurred in a geothermal doublet in the reservoir concluded that some fracture-dominated compartments of the reservoir cannot be modeled using the EPM approach [11] since a previous regional thermo-hydraulic model of Upper Jurassic carbonates [9] failed to predict an early thermal breakthrough. Based on the integration of multi-scale and multi-disciplinary data, Fadel et al.[11] proposed that in fracture-controlled sectors of the reservoir, the discrete fracture network (DFN) approach has to be adopted to appropriately capture the dual-porosity and dual permeability character of the reservoir. Besides, as the Upper Jurassic formation in the North Alpine Foreland Basin deepens towards the Alps, deeper sections of the reservoir are mainly controlled by the hydraulic behavior of faults and fractures, which makes it indispensable to implement them as discrete manifolds [23].

Fracture-controlled reservoirs that need to be modeled using the DFN approach are well known in the published literature to be computationally intensive [10, 16]. In addition, the high heterogeneity and anisotropy involved in such reservoirs pose a serious challenge to geothermal exploration and sustainable reservoir development [30, 15]. In particular, well placement optimization driven by the requirement for maximum sustainable geothermal energy production is a challenging numerical task. Recently, Blank et al. [7] proposed a 2D numerical framework that enables one to find optimal geothermal well placement by maximizing geothermal energy production sustainably. This was the first time authors introduced an efficient numerical framework that involves transient thermo-hydraulic simulation, geothermal multi-well thermo-hydraulic interaction, and a multivariate optimization task. However, the applicability and transferability of the work by Blank et al. is limited to sections of the reservoir that can be modeled as an EPM. Therefore, one of the main purposes of this work is to extend the previously proposed 2D numerical framework to reservoir domains that exhibit more complex permeability structures under non-isothermal conditions. We aim to propose an efficient, open-source numerical framework capable of well placement optimization driven by the requirement for maximum sustainable geothermal energy production in 3D fracture-controlled reservoirs that need to be modeled as a DFN.

To the best of our knowledge, there is no available numerical framework that is efficient enough for performing geothermal multi-well placement optimization based on the requirement for maximum sustainable energy production in 3D fracture-controlled reservoirs. Typically, geothermal well placement optimization tasks would require remeshing after changing well positions, which would be excessively computationally expensive. Motivated by this hindrance, we propose in this work a computational framework that solves this optimization task in a comparatively efficient way.

The paper is structured as follows: Section 3 presents our mathematical model. Section 4 describes how we solve the resulting mathematical problem numerically. Section 5 shows the results of several verification and validation tests conducted with our numerical framework.

3 Mathematical model

Our mathematical model follows from those by Blank et al. [7] and Zinsalo et al. [34]: We model the DFN as a domain $\Omega \in \mathbf{R}^3$ consisting of 3D porous layers denoted by Ω_{la}, porous fractures denoted by Ω_{fr} (with $\Omega_{\mathrm{fr}} \subset \partial\Omega_{\mathrm{la}}$), and wells, where the fractures are 2D manifolds with polygonal boundaries, and the wells are thin cylinders.

Since the radius of a cylindrical well is at least four orders of magnitude smaller than the size of Ω, we model

the wells via the immersed boundary method [31, 7]. That is, we assume that the volumes of the wells are parts of Ω_{la}, and the well-fracture intersections are parts of Ω_{fr} (hence, the wells are physically not there), and we compensate for the absence of the wells by including line mass and energy sink/source terms in areas where the wells should be placed.

In what follows, the objects related to the layers, fractures, and porous rock will be denoted by the subscripts *la*, *fr*, *r*, respectively, in cases in which there may be confusion. The quantities representing the fluid properties do not have any subscripts. We assume that all these components are non-deformable, and they are in local thermal equilibrium with the fluid inside. In addition, only single-phase fluid flow in fully saturated conditions is considered.

3.1 Balance equations

The fluid flow and heat transport in Ω_{la} and Ω_{fr} are modeled by solving the corresponding balance equations for mass, momentum and energy. In Ω_{la}, these equations read, respectively,

$$\varepsilon_r \frac{\partial \rho}{\partial t} + \nabla \cdot (\rho \boldsymbol{v}) = S_{\mathrm{MW}}, \tag{1}$$

$$\boldsymbol{v} = -\frac{1}{\mu}\boldsymbol{k}(\nabla p - \rho \boldsymbol{g}), \tag{2}$$

$$(\rho c)_{\mathrm{eff}} \frac{\partial T}{\partial t} + \rho c_p \boldsymbol{v} \cdot \nabla T - \nabla \cdot (\lambda_{\mathrm{eff}} \nabla T) = S_{\mathrm{EW}}. \tag{3}$$

In (1), ε_r $[-]$ stands for the porosity, ρ $[\mathrm{kg \cdot m^{-3}}]$ represents the density, t $[\mathrm{s}]$ is the time, $\boldsymbol{v}$ $[\mathrm{m \cdot s^{-1}}]$ is the fluid velocity, and S_{MW} $[\mathrm{kg \cdot m^{-3} \cdot s^{-1}}]$ denotes the sum of the mass sources/sinks due to the wells.

In (2), μ $[\mathrm{Pa \cdot s}]$ is the dynamic viscosity of the fluid, and $\boldsymbol{k}$ $[\mathrm{m^2}]$ is the permeability tensor of the rock. We assume $\boldsymbol{k}$ to be generally isotropic and heterogeneous, i.e, $\boldsymbol{k} = k\boldsymbol{I}$, where k is a scalar function, and $\boldsymbol{I}$ is the identity tensor. The quantity p $[\mathrm{Pa}]$ represents the fluid pressure, and $\boldsymbol{g}$ $[\mathrm{m \cdot s^{-2}}]$ denotes the gravitational acceleration vector.

In (3), c_p $[\mathrm{J \cdot kg^{-1} \cdot K^{-1}}]$ is the specific heat at constant pressure of the fluid, T $[\mathrm{K}]$ denotes the common thermodynamic temperature of the fluid and rock, and S_{EW} $[\mathrm{J \cdot m^{-3} \cdot s^{-1}}]$ represents the energy sources/sinks due to the wells.

The subscript *eff* indicates the following combination of the properties of the fluid and rock:

$$\lambda_{\mathrm{eff}} = (1-\varepsilon_r)\lambda_r + \varepsilon_r \lambda, \quad \text{and} \quad (\rho c)_{\mathrm{eff}} = (1-\varepsilon_r)\rho_r c_r + \varepsilon_r \rho c_p, \tag{4}$$

where c_r $[\mathrm{J \cdot kg^{-1} \cdot K^{-1}}]$ stands for the specific heat of the rock, and λ $[\mathrm{W \cdot m^{-1} \cdot K^{-1}}]$ is the thermal conductivity coefficient. The terms S_{MW} and S_{EW} are defined in Section 3.2.

In Ω_{fr}, our equations read

$$d_{\mathrm{fr}}\varepsilon_r \frac{\partial \rho}{\partial t} + d_{\mathrm{fr}} \nabla_{\boldsymbol{t}} \cdot (\rho \boldsymbol{v}) = S_{\mathrm{MW}} + (\rho \boldsymbol{v})_{\mathrm{la}} \cdot \boldsymbol{n}^+ + (\rho \boldsymbol{v})_{\mathrm{la}} \cdot \boldsymbol{n}^-, \tag{5}$$

$$\boldsymbol{v} = -\frac{1}{\mu}\boldsymbol{k}(\nabla_{\boldsymbol{t}} p - \rho \boldsymbol{g}), \tag{6}$$

$$d_{\mathrm{fr}}(\rho c)_{\mathrm{eff}} \frac{\partial T}{\partial t} + d_{\mathrm{fr}} \rho c_p \boldsymbol{v} \cdot \nabla_{\boldsymbol{t}} T - d_{\mathrm{fr}} \nabla_{\boldsymbol{t}} \cdot (\lambda_{\mathrm{eff}} \nabla_{\boldsymbol{t}} T) = S_{\mathrm{EW}} + \boldsymbol{q}_{\mathrm{la}} \cdot \boldsymbol{n}^+ + \boldsymbol{q}_{\mathrm{la}} \cdot \boldsymbol{n}^-, \tag{7}$$

where

$$\boldsymbol{q} = -\left(\lambda_{\mathrm{eff}} \nabla T\right), \tag{8}$$

and the quantities $(\rho\boldsymbol{v})_{\mathrm{la}}\cdot\boldsymbol{n}$ and $\boldsymbol{q}_{\mathrm{la}}\cdot\boldsymbol{n}$ on the right-hand side of (5) and (7) represent the fluxes entering/leaving Ω_{fr} through $\partial\Omega_{\mathrm{la}}$, where $\boldsymbol{n}^+$ and $\boldsymbol{n}^-$ denote the unit outward normals to the fracture ($\boldsymbol{n}^+ + \boldsymbol{n}^- = 0$).

In (5)–(7), d_{fr} [m] is the fracture aperture, which is considered piecewise constant, and the subscript $\boldsymbol{t}$ indicates the derivative in the direction of the unit vector tangential to the fracture. For a scalar-valued function f and a vector-valued function $\boldsymbol{F}$, it holds

$$\nabla_{\boldsymbol{t}} f = \nabla f - \left(\nabla f \cdot \boldsymbol{n}^+\right)\boldsymbol{n}^+ \quad \text{and} \quad \nabla_{\boldsymbol{t}} \cdot \boldsymbol{F} = \left(\boldsymbol{I} - \boldsymbol{n}^+ \otimes \boldsymbol{n}^+\right) : \nabla \boldsymbol{F}.$$

Note that in (5) and (7), the physical units of the source/sink terms are S_{MW} $[\mathrm{kg}\cdot\mathrm{m}^{-2}\cdot\mathrm{s}^{-1}]$ and S_{EW} $[\mathrm{J}\cdot\mathrm{m}^{-2}\cdot\mathrm{s}^{-1}]$, although we denote them by the same symbols as those in (1) and (3).

We assume that p and T are continuous at the interface between the layers and the fractures. This means

$$p_{\mathrm{la}}|_{\partial\Omega_{\mathrm{fr}}} = p_{\mathrm{fr}} \quad \text{and} \quad T_{\mathrm{la}}|_{\partial\Omega_{\mathrm{fr}}} = T_{\mathrm{fr}}. \tag{9}$$

On the boundaries $\partial\Omega_{\mathrm{la}}$ and $\partial\Omega_{\mathrm{fr}}$, we consider the Dirichlet boundary conditions for p and T and the flux boundary conditions

$$\rho\boldsymbol{v}\cdot\boldsymbol{n} = q_{\mathrm{M}} \quad \text{and} \quad \boldsymbol{q}\cdot\boldsymbol{n} = q_{\mathrm{E}}. \tag{10}$$

In Ω_{la}, conditions (10) will be prescribed on parts $\Gamma_{\partial\mathrm{la,M,flux}}$ and $\Gamma_{\partial\mathrm{la,E,flux}}$ of $\partial\Omega_{\mathrm{la}}$, respectively. In Ω_{fr}, we set $q_{\mathrm{M}} = q_{\mathrm{E}} = 0$ on the whole $\partial\Omega_{\mathrm{fr}}$.

Every intersection of N fractures $\omega_1, \ldots, \omega_N$ is assumed to be a line segment. Denoting $\boldsymbol{n}^s_{\partial i}$ the unit outward normal corresponding to the side $s \in \{+,-\}$ of this intersection inside the fracture ω_i, we prescribe

$$\sum_{i\in\{1,2\}}\sum_{s\in\{+,-\}} d_{\mathrm{fr},i}(\rho\boldsymbol{v})_{\mathrm{fr}}\cdot\boldsymbol{n}^s_{\partial i} = 0 \qquad \text{and} \qquad \sum_{i\in\{1,2\}}\sum_{s\in\{+,-\}} d_{\mathrm{fr},i}\boldsymbol{q}_{\mathrm{fr}}\cdot\boldsymbol{n}^s_{\partial i} = 0. \tag{11}$$

In our numerical framework, the primary variables for solving the balance equations are p and T. The fluid properties ρ, μ, c_p and λ are generally considered p- and T-dependent. The parameters of the porous matrix are considered spatial-dependent in Ω_{la}. In Ω_{fr}, they are fracture-dependent constants. However, for simplicity, the simulations presented in Section 5 will be carried out only for constant μ, c_p and λ. Those in Section 5.2, we will consider even constant ρ.

The balance equations will be solved on the time interval $[t_{\mathrm{ini}}, t_{\mathrm{fin}}]$. The initial conditions for p and T will be denoted by p_{ini} and T_{ini}.

3.2 Wells

We consider 2 types of wells: an injection well (which acts as a source) and a production well (which acts as a sink). Our model for them is basically an extension of that one by Blank et al.[7] from 2D to 3D. That is, employing the immersed boundary method, we define the source/sink terms S_{MW} and S_{EW} as line sources/sinks first. Afterward, we approximate them using the non-matching approach [31, 7] to make their subsequent numerical approximation less mesh-dependent.

Each well w is modeled as a cylinder $\boldsymbol{S}_w$ with the height H_w [m], radius r_w [m], and flow rate Q_w $[\mathrm{m}^3\cdot\mathrm{s}^{-1}]$ of a fluid with the density ρ_w $[\mathrm{kg}\cdot\mathrm{m}^{-3}]$, temperature T_w [K], and specific heat capacity at constant pressure $c_{p,w}$ $[\mathrm{J}\cdot\mathrm{kg}^{-1}\cdot\mathrm{K}^{-1}]$. Q_w is positive for an injection well and negative for a production well.

We assume the boundary of each intersection of a fracture and a well to be an ellipse with the center $\boldsymbol{S}_{\mathrm{e}}$ and semi-axes of the lengths L_1 [m] and L_2 [m]. The intersection is equipped with a local coordinate system given by $\boldsymbol{S}_{\mathrm{e}}$ and an orthonormal basis consisting of vectors parallel with the above semi-axes. For a point $\boldsymbol{x}$ lying in the considered fracture, we define

$$\|\boldsymbol{x}\|_{\mathsf{inter}} = \sqrt{\frac{L_2^2\,|x_1|^2 + L_1^2\,|x_2|^2}{L_1 L_2}}, \tag{12}$$

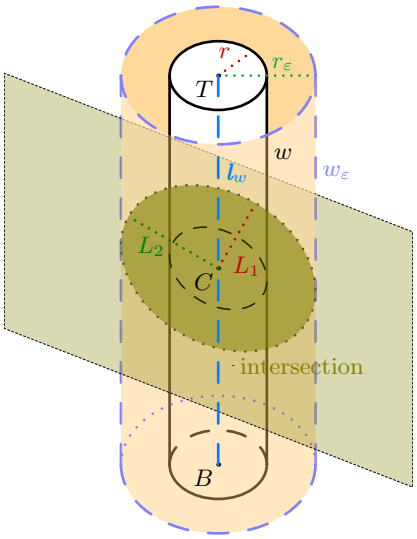

Figure 2: Well w and its artificial extension w_ε cut by a fracture that divides both w and w_ε into 3 segments $\boldsymbol{S}_{w,1}$, $\boldsymbol{S}_{w,2}$, and $\boldsymbol{S}_{w,3}$ with the heights $H_{w,1} = |TC|$, $H_{w,2} = |CB|$, and $H_{w,3} =$ fracture aperture, where the points T, B, and C are the centers of the top and bottom of w, and the center of the intersection, respectively. Since $|TB| \gg H_{w,3}$, the fact that $H_{w,1}+H_{w,2}+H_{w,3} > |TB|$ is negligible. $\boldsymbol{l}_w$ is the line segment connecting the points T and B.

where x_1 and x_2 are the coordinates of $\boldsymbol{x}$ in the above basis. Hence, the intersection is formed by points $\boldsymbol{x}$ in the fracture satisfying $\|\boldsymbol{x} - \boldsymbol{S}_\mathrm{e}\|_\mathrm{inter} \leq \sqrt{L_1 L_2}$.

Although such an intersection has zero thickness, we assume in the following computations that its thickness is d_fr, the fracture aperture. These intersections divide a well w (see Figure 2) into $N_{w,\mathrm{la}}$ segments $S_{w,1}, \ldots, \boldsymbol{S}_{w,N_\mathrm{la}}$ in Ω_la and into N_fr segments $\boldsymbol{S}_{w,N_\mathrm{la}+1}, \ldots, \boldsymbol{S}_{w,N_\mathrm{la}+N_\mathrm{fr}}$ in Ω_fr. We may define additional segments in Ω_la to increase the precision of the model, e.g., if the porous medium is highly heterogeneous. The segments have the heights $H_{w,1}, \ldots, H_{w,N_\mathrm{la}+N_\mathrm{fr}}$, respectively, where the heights of the segments in Ω_la are measured along the line segment $\boldsymbol{l}_w$ in Figure 2. This divides the flow rate Q_w into $N_w := N_{w,\mathrm{la}} + N_{w,\mathrm{fr}}$ portions Q_i ($Q_w = \sum_{i=1}^{N_w} Q_{w,i}$) that are approximated based on the lateral surface area $|\boldsymbol{S}_{w,i}|$ and permeability $\boldsymbol{k}_{w,i}$ of the segments as follows:

$$Q_{w,i} = \boldsymbol{k}_{w,i}\,|\boldsymbol{S}_{w,i}|\,C \quad \text{for} \quad C = Q_w/(\boldsymbol{k}_\mathrm{avr}\,|\boldsymbol{S}_\mathrm{tot}|),$$

where

$$|\boldsymbol{S}_\mathrm{tot}| = \sum_{i=1}^{N_w} |\boldsymbol{S}_{w,i}| \quad \text{and} \quad \boldsymbol{k}_\mathrm{avr} = \sum_{i=1}^{N_w} \boldsymbol{k}_{w,i}\,|\boldsymbol{S}_{w,i}|\,/\,|\boldsymbol{S}_\mathrm{tot}|\,. \tag{13}$$

Using the portions $Q_{w,i}$, the source/sink terms in our balance equations are approximated as

$$S_\mathrm{MW} = \sum_{w \in \mathcal{W}_\mathrm{inj} \cup \mathcal{W}_\mathrm{pro}} \rho_w C_w \delta_w \quad \text{and} \quad S_\mathrm{EW} = C_\mathrm{pen} \sum_{w \in \mathcal{W}_\mathrm{inj}} C_w (\rho c_p)_w \,(T_w - T)\,\delta_w, \tag{14}$$

where $\mathcal{W}_\mathrm{inj}$ and $\mathcal{W}_\mathrm{pro}$ are the sets of the injection and production wells, respectively, δ_w [m^{-2}] denotes the Dirac delta function, and C_pen [-] is a positive penalty parameter. Setting C_pen to a large value makes S_EW in (3) and (7) dominant, enforcing $T \approx T_w$. The functions C_w [m^2/s] in Ω_la and C_w [m^3/s] in Ω_fr depend only on the portions $Q_{w,i}$ and the shape of the segments $\boldsymbol{S}_{w,i}$. Both C_w and δ_w are defined in Sections 3.2.1 and 3.2.2.

3.2.1 C_w and δ_w for wells in Ω_{la}

In Ω_{la}, we consider δ_w to be the Dirac delta function with respect to the line segment $\boldsymbol{l}_w$ in Figure 2. Thus, $\int_{\boldsymbol{S}_w} \delta_w = H_w = \sum_{i=1}^{N_{w,\mathrm{la}}} H_{w,i}$.

To apply the non-matching approach, we surround w by an artificial well w_ε (see Figure 2) with the artificial radius r_ε [m] ($r_\varepsilon \gg r_w$), and we approximate δ_w via

$$\delta_w(\boldsymbol{x}) \approx \frac{\pi}{r_\varepsilon^2\,(\pi^2-4)}\theta\left(\frac{\mathrm{dist}(\boldsymbol{x},\boldsymbol{l}_w)}{r_\varepsilon}\right)\mathcal{I}_{\boldsymbol{S}_{w_\varepsilon}}(\boldsymbol{x}), \tag{15}$$

where θ is the cut-off function

$$\theta(x) = \begin{cases} \cos(\pi x)+1, & x<1 \\ 0, & \text{otherwise} \end{cases}, \tag{16}$$

$\mathrm{dist}(\boldsymbol{x},\boldsymbol{l}_w)$ denotes the distance between $\boldsymbol{x}$ and $\boldsymbol{l}_w$, and $\mathcal{I}_{\boldsymbol{S}_{w_\varepsilon}}$ represents the indicator function of the artificial cylinder $\boldsymbol{S}_{w_\varepsilon}$ corresponding to w_ε.

The function C_w is defined as

$$C_w = \sum_{i=1}^{N_{w,\mathrm{la}}} C_{w,i}\mathcal{I}_{\boldsymbol{S}_{w_\varepsilon,i}}, \tag{17}$$

where $\mathcal{I}_{\boldsymbol{S}_{w_\varepsilon,i}}$ is the indicator function of $\boldsymbol{S}_{w_\varepsilon,i}$, and each $C_{w,i}$ $[\mathrm{m}^2/\mathrm{s}]$ is a constant computed as follows:

In steady-state, (1) reduces to $\nabla\cdot(\rho\boldsymbol{v}) = S_{\mathrm{MW}}$. Integrating both sides of this equation over $\boldsymbol{S}_w$, applying the Gauss theorem, and neglecting the flow through the bases of $\boldsymbol{S}_w$ yields

$$\int_{\boldsymbol{S}_w}\nabla\cdot(\rho\boldsymbol{v}) = \int_{\partial\boldsymbol{S}_w}\rho\boldsymbol{v}\cdot\boldsymbol{n} \approx \sum_{i=1}^{N_{w,\mathrm{la}}}(\rho\boldsymbol{v})|_{\boldsymbol{S}_{w,i}}\cdot|\boldsymbol{S}_{w,i}| = \sum_{i=1}^{N_{w,\mathrm{la}}}\rho_{w,i}Q_{w,i}, \tag{18}$$

where we set $v|_{\boldsymbol{S}_{w,i}} = Q_{w,i}/\left|\boldsymbol{S}_{w,i}\right|$, and

$$\int_{\boldsymbol{S}_w} S_{\mathrm{MW}} = \int_{\boldsymbol{S}_w}\sum_{w'\in\mathcal{W}_{\mathrm{inj}}\cup\mathcal{W}_{\mathrm{pro}}}\rho_{w'}C_{w'}\delta_{w'} = \int_{\boldsymbol{S}_w}\rho_w C_w\delta_w = \sum_{i=1}^{N_{w,\mathrm{la}}}\rho_{w,i}C_{w,i}H_{w,i}. \tag{19}$$

Comparing both integrals reveals $C_{w,i} = Q_{w,i}/H_{w,i}$.

3.2.2 C_w and δ_w for wells in Ω_{fr}

For an intersection of a fracture with a well w, δ_w is the Dirac delta function with respect to the center of the intersection (the point C in Figure 2). Similarly as in Section 3.2.1, we utilize the artificial well w_ε to approximate δ_w as

$$\delta_w(\boldsymbol{x}) \approx \frac{\pi}{L_{1,\varepsilon}L_{2,\varepsilon}\,(\pi^2-4)}\theta\left(\frac{\|\boldsymbol{x}-\boldsymbol{S}_{\mathrm{e}}\|_{\mathrm{inter}}}{\sqrt{L_{1,\varepsilon}L_{2,\varepsilon}}}\right)\mathcal{I}_{\boldsymbol{S}_{w_\varepsilon}}(\boldsymbol{x}), \tag{20}$$

where $L_{1,\varepsilon}$ and $L_{2,\varepsilon}$ are the artificial lengths of the semi-axes ($L_{1,\varepsilon}\gg L_1$, $L_{2,\varepsilon}\gg L_2$), θ and $\mathcal{I}_{\boldsymbol{S}_{w_\varepsilon}}$ have the same meaning as in (15), and $\|\cdot\|_{\mathrm{inter}}$ is defined by (12). We set

$$C_w = \sum_{i=N_{w,\mathrm{la}}+1}^{N_w} C_{w,i}\mathcal{I}_{\boldsymbol{S}_{w_\varepsilon,i}}. \tag{21}$$

Assuming that the intersection has the thickness d_{fr}, the constants $C_{w,i}$ $[\mathrm{m}^3/\mathrm{s}]$ are computed similarly as in Section 3.2.1 to be $C_{w,i} = Q_{w,i}$.

3.3 Optimization

We assume that for a given time interval $[t_{\mathrm{ini}}, t_{\mathrm{fin}}]$, the optimal placement of the wells is the one maximizing the power $\mathcal{P}$ [W] of the geothermal facility that we compute using the following formulas from Blank et al.[7]. For given sets of injection and production wells $\mathcal{W}_{\mathrm{inj}}$ and $\mathcal{W}_{\mathrm{pro}}$, we set

$$\mathcal{P}(\mathcal{W}_{\mathrm{inj}}, \mathcal{W}_{\mathrm{pro}}) = \frac{1}{t_{\mathrm{fin}} - t_{\mathrm{ini}}} \int_{t_{\mathrm{ini}}}^{t_{\mathrm{fin}}} \left(E_{\mathsf{prod}}(t, \mathcal{W}_{\mathrm{inj}}, \mathcal{W}_{\mathrm{pro}}) - E_{\mathsf{pump}}(t, \mathcal{W}_{\mathrm{inj}}, \mathcal{W}_{\mathrm{pro}})\right) \mathrm{d}t, \tag{22}$$

where E_{prod} [J/s] denotes the flux of energy through the wells,

$$E_{\mathsf{prod}}(t, \mathcal{W}_{\mathrm{inj}}, \mathcal{W}_{\mathrm{pro}}) = \sum_{w \in \mathcal{W}_{\mathrm{pro}}} (\rho c_p T)|_w(t) \, |Q_w| - \sum_{w \in \mathcal{W}_{\mathrm{inj}}} \rho_w c_{p,w} T_w Q_w, \tag{23}$$

and E_{pump} [J/s] stands for the energy needed for the operation of the water pumps,

$$E_{\mathsf{pump}}(t, \mathcal{W}_{\mathrm{inj}}, \mathcal{W}_{\mathrm{pro}}) = \sum_{w \in \mathcal{W}_{\mathrm{inj}} \cup \mathcal{W}_{\mathrm{pro}}} \frac{|Q_w|}{\varepsilon_w} \left| \Delta p|_w(t) \right|. \tag{24}$$

In (24), ε_w [-] represents the efficiency of the pump, and $\Delta p|_w$ [Pa] denotes the average of $p - p_{\mathrm{ini}}$ over $\boldsymbol{S}_w$.

4 Numerical schemes

This section describes how we solve the balance equations and optimization problem numerically.

4.1 Balance equations

We solve our balance equations via a numerical scheme that combines the semi-implicit time discretization with the finite element method (FEM), considering P_1 elements both for p and T. The primary reason for using the semi-implicit time discretization and P_1 elements is to reduce the computational costs because each evaluation of the power $\mathcal{P}$ during the optimization requires the solution of the balance equations over $[t_{\mathrm{ini}}, t_{\mathrm{fin}}]$. To stabilize the resulting numerical scheme, we employ the algebraic flux correction (AFC), which we consider an easy and effective stabilization method for transport problems [4, 17].

To carry out the time discretization in Ω_{la}, we denote the value of a function f at time t^n by f^n (where $t_{\mathrm{ini}} = t^0$ and $t_{\mathrm{fin}} = t^{N_t}$ for $N_t \in \mathbb{N}$), and we set $\Delta t^n := t^{n+1} - t^n$. Considering (1)–(3) at time t^{n+1}, using the chain rule for $\partial\rho/\partial t$, approximating the time derivatives by the backward differences, replacing some terms from t^{n+1} with their counterparts from time t^n to get a linear scheme for p and T, and employing a Taylor expansion for ρ^{n+1}, leads to

$$\varepsilon_r \left(\frac{\partial \rho}{\partial p}\right)^n \frac{p^{n+1} - p^n}{\Delta t^n} + \varepsilon_r \left(\frac{\partial \rho}{\partial T}\right)^n \frac{T^{n+1} - T^n}{\Delta t^n} + \nabla \cdot (\rho^n \boldsymbol{v}^{n+1}) = S_{\mathrm{MW}}^{n+1}, \tag{25}$$

$$(\rho c)_{\mathrm{eff}}^n \frac{T^{n+1} - T^n}{\Delta t^n} + \rho^n c_p^n \boldsymbol{v}^n \cdot \nabla T^{n+1} - \nabla \cdot \left(\lambda_{\mathrm{eff}}^n \nabla T^{n+1}\right) = S_{\mathrm{EW}}^{n+1}, \tag{26}$$

where

$$\boldsymbol{v}^{n+1} = -\frac{1}{\mu^n} \boldsymbol{k} \left(\nabla p^{n+1} - \rho^{n+1} \boldsymbol{g}\right), \tag{27}$$

$$S_{\mathrm{MW}}^{n+1} = \sum_{w \in \mathcal{W}_{\mathrm{inj}} \cup \mathcal{W}_{\mathrm{pro}}} \rho^{n+1} C_w \delta_w, \tag{28}$$

$$S_{\mathrm{EW}}^{n+1} = C_{\mathrm{pen}} \sum_{w \in \mathcal{W}_{\mathrm{inj}}} C_w (\rho c_p)_w \left(T_w - T^{n+1}\right) \delta_w, \tag{29}$$

$$\rho^{n+1} = \rho^n + \Delta t^n \left(\left(\frac{\partial \rho}{\partial p}\right)^n \frac{p^{n+1} - p^n}{\Delta t^n} + \left(\frac{\partial \rho}{\partial T}\right)^n \frac{T^{n+1} - T^n}{\Delta t^n} \right). \tag{30}$$

Hence, in every time step, we solve (26) first to obtain T^{n+1}. Afterward, we solve (25) to get p^{n+1}.

The spatial discretization via the FEM is carried out in the ordinary way: We derive the weak formulation by multiplying each term in (25) and (26) by a test function, integrating the result over Ω_{la}, and applying the Gauss theorem and the boundary conditions (10) to the last term on each left-hand side.

In Ω_{fr}, we employ the same procedure as for (1)–(3) to discretize (5)–(7), but we also utilize (11).

Afterward, we triangulate Ω_{la} by a boundary-conforming mesh of tetrahedra and Ω_{fr} by a boundary-conforming mesh of triangles, where each triangle in Ω_{fr} is a face of a tetrahedron in Ω_{la}. Then, we approximate all functions using the corresponding P_1 elements.

Denoting the test functions by φ_h, the finite element approximation of a function by the subscript h, and the standard inner products in $L^2(\Omega_{\mathrm{la}})$, $L^2(\Omega_{\mathrm{fr}})$, $L^2(\partial\Omega_{\mathrm{la}})$ and $L^2(\partial\Omega_{\mathrm{fr}})$ by $(\cdot,\cdot)_{\mathrm{la}}$, $(\cdot,\cdot)_{\mathrm{fr}}$, $(\cdot,\cdot)_{\partial\mathrm{la}}$ and $(\cdot,\cdot)_{\partial\mathrm{fr}}$, respectively, we obtain

$$\begin{aligned}&\left(\varepsilon_{r,h}\left(\frac{\partial\rho}{\partial p}\right)_h^n\frac{p_h^{n+1}-p_h^n}{\Delta t^n},\,\varphi_{h,\mathrm{la}}\right)_{\mathrm{la}}+\left(\varepsilon_{r,h}\left(\frac{\partial\rho}{\partial T}\right)_h^n\frac{T_h^{n+1}-T_h^n}{\Delta t^n},\,\varphi_{h,\mathrm{la}}\right)_{\mathrm{la}}\\&+\left(q_{\mathrm{M},h}^{n+1},\,\varphi_{h,\mathrm{la}}\right)_{\Gamma_{\partial\mathrm{la,M,flux}}}-\left(\rho_h^n,\boldsymbol{v}_h^{n+1}\cdot\nabla\varphi_{h,\mathrm{la}}\right)_{\mathrm{la}}=\left(S_{\mathrm{MW},h}^{n+1},\,\varphi_{h,\mathrm{la}}\right)_{\mathrm{la}},\end{aligned}\tag{31}$$

$$\begin{aligned}&\left((\rho c)_{h,\mathrm{eff}}^n\frac{T_h^{n+1}-T_h^n}{\Delta t^n},\,\varphi_{h,\mathrm{la}}\right)_{\mathrm{la}}+\left(\rho_h^n c_{p,h}^n\boldsymbol{v}_h^n\cdot\nabla T_h^{n+1},\,\varphi_{h,\mathrm{la}}\right)_{\mathrm{la}}\\&+\left(q_{\mathrm{E},h}^{n+1},\,\varphi_{h,\mathrm{la}}\right)_{\Gamma_{\partial\mathrm{la,E,flux}}}+\left(\lambda_{h,\mathrm{eff}}^n,\nabla T_h^{n+1}\cdot\nabla\varphi_{h,\mathrm{la}}\right)_{\mathrm{la}}=\left(S_{\mathrm{EW},h}^{n+1},\,\varphi_{h,\mathrm{la}}\right)_{\mathrm{la}},\end{aligned}\tag{32}$$

$$\begin{aligned}&\left(d_{\mathrm{fr},h}\varepsilon_{r,h}\left(\frac{\partial\rho}{\partial p}\right)_h^n\frac{p_h^{n+1}-p_h^n}{\Delta t^n},\,\varphi_{h,\mathrm{fr}}\right)_{\mathrm{fr}}+\left(d_{\mathrm{fr},h}\varepsilon_{r,h}\left(\frac{\partial\rho}{\partial T}\right)_h^n\frac{T_h^{n+1}-T_h^n}{\Delta t^n},\,\varphi_{h,\mathrm{fr}}\right)_{\mathrm{fr}}\\&+\left(d_{\mathrm{fr},h}q_{\mathrm{M},h}^{n+1},\,\varphi_{h,\mathrm{fr}}\right)_{\Gamma_{\partial\mathrm{fr,M,flux}}}-\left(d_{\mathrm{fr},h}\rho_h^n,\boldsymbol{v}_h^{n+1}\cdot\nabla_{\boldsymbol{t}}\varphi_{h,\mathrm{fr}}\right)_{\mathrm{fr}}\\&=\left(S_{\mathrm{MW},h}^{n+1},\,\varphi_{h,\mathrm{fr}}\right)_{\mathrm{fr}}+\left((\rho\boldsymbol{v})_{h,\mathrm{la}}\cdot\boldsymbol{n}^+ +(\rho\boldsymbol{v})_{h,\mathrm{la}}\cdot\boldsymbol{n}^-,\,\varphi_{h,\mathrm{fr}}\right)_{\mathrm{fr}},\end{aligned}\tag{33}$$

$$\begin{aligned}&\left(d_{\mathrm{fr},h}(\rho c)_{h,\mathrm{eff}}^n\frac{T_h^{n+1}-T_h^n}{\Delta t^n},\,\varphi_{h,\mathrm{fr}}\right)_{\mathrm{fr}}+\left(d_{\mathrm{fr},h}\rho_h^n c_{p,h}^n\boldsymbol{v}_h^n\cdot\nabla_{\boldsymbol{t}}T_h^{n+1},\,\varphi_{h,\mathrm{fr}}\right)_{\mathrm{fr}}\\&+\left(d_{\mathrm{fr},h}q_{\mathrm{E},h}^{n+1},\,\varphi_{h,\mathrm{fr}}\right)_{\Gamma_{\partial\mathrm{fr,E,flux}}}+\left(d_{\mathrm{fr},h}\lambda_{h,\mathrm{eff}}^n,\nabla_{\boldsymbol{t}}T_h^{n+1}\cdot\nabla_{\boldsymbol{t}}\varphi_{h,\mathrm{fr}}\right)_{\mathrm{fr}}\\&=\left(S_{\mathrm{EW},h}^{n+1},\,\varphi_{h,\mathrm{fr}}\right)_{\mathrm{fr}}+\left(\boldsymbol{q}_{h,\mathrm{la}}\cdot\boldsymbol{n}^+ +\boldsymbol{q}_{h,\mathrm{la}}\cdot\boldsymbol{n}^-,\,\varphi_{h,\mathrm{fr}}\right)_{\mathrm{fr}}\end{aligned}\tag{34}$$

for all $\varphi_{h,\mathrm{la}}$ and $\varphi_{h,\mathrm{fr}}$.

We add each equation (33) for the test function $\varphi_{h,i,\mathrm{fr}}$ to each equation (31) for the test function $\varphi_{h,j,\mathrm{la}}$ if the supports of $\varphi_{h,i,\mathrm{fr}}$ and $\varphi_{h,j,\mathrm{la}}$ overlap. This means that the integrals in equations in (33) containing $(\rho\boldsymbol{v})_{h,\mathrm{la}}\cdot\boldsymbol{n}^{\pm}$ and the integrals over $\Omega_{\mathrm{fr}}\subset\partial\Omega_{\mathrm{la}}$ in equations in (31) cancel each other. For (32) and (34), we do the same, which results in the same cancellation of integrals.

We denote the sets of equations obtained by modifying (31) and (32) in the aforementioned way by EM_{la} and EE_{la}, respectively.

The next step of the discretization procedure is the application of the AFC to the system EE_{la}, where the new system will be denoted by $\overline{EE}_{\mathrm{la}}$. We apply it only to EE_{la} because EM_{la} does not need any stabilization.

The AFC requires that EE_{la} is written in the vector form

$$\boldsymbol{M}\left((1/\Delta t^n)(\boldsymbol{u}^{n+1}-\boldsymbol{u}^n)\right)+\boldsymbol{A}\boldsymbol{u}^{n+1}=\boldsymbol{F}, \tag{35}$$

where $\boldsymbol{u}$ represents the solution vector, and $\boldsymbol{M}$ and $\boldsymbol{A}$ are the matrices of the coefficients in front of the components of $\boldsymbol{u}^{n+1}$. $\boldsymbol{M}$ contains all coefficients originating from the approximation of the time derivatives, and $\boldsymbol{A}$ contains the rest. All remaining terms are in the vector $\boldsymbol{F}$.

The components $\boldsymbol{M}_{i,j}$, $\boldsymbol{A}_{i,j}$, and $\boldsymbol{F}_i$ of the matrices $\boldsymbol{M}$, $\boldsymbol{A}$, and the vector $\boldsymbol{F}$ can be calculated to be

$$\begin{aligned}\boldsymbol{M}_{i,j}=&\left(\left(\varepsilon_{r,h}\rho_h^n c_{p,h}^n+(1-\varepsilon_{r,h})\rho_{r,h}c_{r,h}\right)\varphi_{h,j,\mathrm{la}},\varphi_{h,i,\mathrm{la}}\right)_{\mathrm{la}}\\&+\left(\left(\varepsilon_{r,h}\rho_h^n c_{p,h}^n+(1-\varepsilon_{r,h})\rho_{r,h}c_{r,h}\right)\varphi_{h,j,\mathrm{fr}},d_{\mathrm{fr},h}\varphi_{h,i,\mathrm{fr}}\right)_{\mathrm{fr}},\end{aligned} \tag{36}$$

$$\begin{aligned}\boldsymbol{A}_{ij}=&\left(\rho_h^n c_{p,h}^n\boldsymbol{v}_h^n\cdot\nabla\varphi_{h,j,\mathrm{la}},\varphi_{h,i,\mathrm{la}}\right)_{\mathrm{la}}+\left(\lambda_{h,\mathrm{eff}}^n,\nabla\varphi_{h,j,\mathrm{la}}\cdot\nabla\varphi_{h,i,\mathrm{la}}\right)_{\mathrm{la}}\\&+\left(d_{\mathrm{fr},h}\rho_h^n c_{p,h}^n\boldsymbol{v}_h^n\cdot\nabla_{\boldsymbol{t}}\varphi_{h,j,\mathrm{fr}},\varphi_{h,i,\mathrm{fr}}\right)_{\mathrm{fr}}+\left(\lambda_{h,\mathrm{eff}}^n d_{\mathrm{fr},h},\nabla_{\boldsymbol{t}}\varphi_{h,j,\mathrm{fr}}\cdot\nabla_{\boldsymbol{t}}\varphi_{h,i,\mathrm{fr}}\right)_{\mathrm{fr}}\\&+\left(C_{\mathrm{pen}}\sum_{w\in\mathcal{W}_{\mathrm{inj}}}C_w(\rho c_p)_w\delta_w\varphi_{h,j,\mathrm{la}},\varphi_{h,i,\mathrm{la}}\right)_{\mathrm{la}}+\left(C_{\mathrm{pen}}\sum_{w\in\mathcal{W}_{\mathrm{inj}}}C_w(\rho c_p)_w\delta_w\varphi_{h,j,\mathrm{fr}},\varphi_{h,i,\mathrm{fr}}\right)_{\mathrm{fr}},\end{aligned} \tag{37}$$

$$\begin{aligned}\boldsymbol{F}_i=&-\left(q_{\mathrm{E},h}^{n+1},\varphi_{h,i,\mathrm{la}}\right)_{\partial\mathrm{la,E,flux}}+\left(C_{\mathrm{pen}}\sum_{w\in\mathcal{W}_{\mathrm{inj}}}C_w(\rho c_p)_w T_w\delta_w,\varphi_{h,i,\mathrm{la}}\right)_{\mathrm{la}}\\&-\left(d_{\mathrm{fr},h}q_{\mathrm{E},h}^{n+1},\varphi_{h,i,\mathrm{fr}}\right)_{\partial\mathrm{fr,E,flux}}+\left(C_{\mathrm{pen}}\sum_{w\in\mathcal{W}_{\mathrm{inj}}}C_w(\rho c_p)_w\delta_w T_w,\varphi_{h,i,\mathrm{fr}}\right)_{\mathrm{fr}}.\end{aligned} \tag{38}$$

Once $\boldsymbol{M}$, $\boldsymbol{A}$, and $\boldsymbol{F}$ are known, the application of the AFC consists of modifying

1. $\boldsymbol{M}$ by applying mass lumping,
2. $\boldsymbol{A}$ by adding artificial diffusion in such a way that $\boldsymbol{A}$ becomes an M-matrix,
3. $\boldsymbol{F}$ by adding carefully designed anti-diffusive fluxes that compensate for the excessive diffusion in $\boldsymbol{A}$ in regions where the solution is expected to be smooth.

We perform this via the algorithm with the Zalesak limiter[4, 17], which does not contain any user-defined tuning parameters.

At the end, we modify EM_{la} and $\overline{EE}_{\mathrm{la}}$ by utilizing conditions (9) to prescribe p and T at mesh nodes on $\partial\Omega_{\mathrm{la}}$ that coincide with nodes in $\overline{\Omega}_{\mathrm{fr}}$, and by employing the Dirichlet boundary conditions. Then, we solve the resulting systems of linear algebraic equations.

4.2 Wells and optimization

When computing the average permeability $\boldsymbol{k}_{\mathrm{avr}}$ in (13), the permeability $\boldsymbol{k}_{w,i}$ of a segment $\boldsymbol{S}_{w,i}$ is computed as follows:

- For $\boldsymbol{S}_{w,i}\subset\Omega_{\mathrm{fr}}$, we set $\boldsymbol{k}_{w,i}=(1/N_P)\sum_{j=1}^{N_P}\boldsymbol{k}(P_j)$, where the points P_j are given in Figure 3, and $N_P\in\mathbb{N}$ is a fixed number that is the same for all $\boldsymbol{S}_{w,i}$.

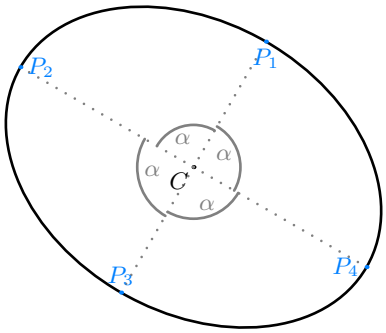

Figure 3: Definition of points $P_1, \ldots, P_{N_P}$ for $N_P = 4$ for a well-fracture intersection $\boldsymbol{S}_{w,i} \subset \Omega_{\mathrm{fr}}$. The coordinates of the vector $\overrightarrow{CP_1}$ in the local base used in (12) are $(L_1, 0)$. The angle is $\alpha = 360°/N_P$.

- Each $\boldsymbol{S}_{w,i} \subset \Omega_{\mathrm{la}}$ corresponds to a part of $\boldsymbol{l}_w$ between certain points B and C (e.g., those in Figure 2). The intersection of $\boldsymbol{S}_w$ with a plane that is perpendicular to $\boldsymbol{S}_w$ and goes through the midpoint of the line segment $\overline{BC}$ is a circle on which we can define points $P_1, \ldots, P_{N_P}$ in the same way as on the ellipse in Figure 3. With these points, we set $\boldsymbol{k}_{w,i} = (1/N_P) \sum_{j=1}^{N_P} \boldsymbol{k}(P_j)$. Again, N_P has the same value for all $\boldsymbol{S}_{w,i}$.

The average $T|_w$ in (23) at time t is computed as the weighted average of the values $T(t, P_j)$ for all P_j from the previous paragraph, where the weight of $T(t, P_j)$ for $P_j \in \boldsymbol{S}_{w,i}$ is $|Q_{w,i}| \,/\, \left(N_p \sum_{k=1}^{N_w} |Q_{w,k}|\right)$. The averages $\rho|_w$ and $c_p|_w$ in (23), and $\Delta p|_w$ in (24) are computed in the same way as $T|_w$.

The integral in (22) is computed via the trapezoidal rule with the step Δt^n from Section 4.1.

As for the problem of maximizing the power $\mathcal{P}$ for a given definition of $\mathcal{P}$, we solve it via gradient-free global optimization algorithms from the library NLopt[18]. Specifically, we will show the results for two deterministic algorithms:

- DIRECT, which searches for the optimum by dividing the parametric space into hyperrectangles of decreasing size,
- the AGS, which approximates the parametric space via the Hilbert curve that is searched iteratively by utilizing the information from previous iterations.

In the NLopt, the AGS is the only gradient-free global optimization algorithm that supports nonlinear constraints and evaluates the objective function only at feasible points. Hence, it is our only choice if the optimization problem description leads to nonlinear constraints.

5 Verification and validation

The following sections describe several tests that we carried out to verify and validate our optimization framework. Unless stated otherwise, all physical quantities mentioned here are in the SI units, which correspond to the units stated in Section 3.

We implemented the numerical solver in C++ using Deal.II[1] and NLopt[18], and performed the computations sequentially on the computer HPE Synergy 480 Gen10 Plus with 2 Xeon eighteen-core processors, 3000 MHz, 768 GB RAM. The computer models of the spatial domains used in this section were created using Frackit[14] and visualized using VisIt[8] and ParaView[3]. The spatial meshes were generated using Gmsh[13] and TetGen[32].

5.1 Test of solver for fluid flow and heat transport

We tested the numerical solver for the fluid flow and heat transport through a convergence study with a prescribed analytical solution and realistic values of physical parameters.

The domain considered in this test is depicted in Figure 4: It consists of a reservoir containing 3 fractures of different populations and two wells. The corresponding constant material properties and the other parameter values are listed in Table 1. The density was defined as by Zinsalo et al.[34]:

$$\rho(T) = 1.0335 \cdot 10^{-5} T^3 - 0.01339 T^2 + 4.9692 T + 432.2571. \tag{39}$$

The problem was solved for $t_{\mathrm{ini}} = 0$ s and $t_{\mathrm{fin}} = 60 \cdot 60 \cdot 24 \cdot 365$ s ≈ 1 year.

On the right-hand sides of (1), (3), (5), and (7), we added additional sources S_{M} and S_{E} that assure that the resulting system has the solution

$$\begin{aligned} p_{\mathrm{ana}}(t,x,y,z) = \sin\left(4\pi x/l_{\mathrm{sc}} - \pi/2\right) \cdot \sin\left(4\pi y/l_{\mathrm{sc}} - \pi/2\right) \cdot \sin\left(\pi(z+3200)/(l_{\mathrm{sc}} \cdot 0.3)\right) \\ \cdot \sin\left(0.5\pi t/(t_{\mathrm{fin}} - t_{\mathrm{ini}})\right) \cdot p_{\mathrm{mult}} + p_{\mathrm{shift}} - p_{\mathrm{grad}} \cdot (z+3200)/l_{\mathrm{sc}}, \end{aligned} \tag{40}$$

$$\begin{aligned} T_{\mathrm{ana}}(t,x,y,z) = \sin\left(4\pi x/l_{\mathrm{sc}} - \pi/2\right) \cdot \sin\left(4\pi y/l_{\mathrm{sc}} - \pi/2\right) \cdot \sin\left(\pi(z+3200)/(l_{\mathrm{sc}} \cdot 0.3)\right) \\ \cdot \sin\left(0.5\pi t/(t_{\mathrm{fin}} - t_{\mathrm{ini}})\right) \cdot T_{\mathrm{mult}} + T_{\mathrm{shift}} - T_{\mathrm{grad}} \cdot (z+3200)/l_{\mathrm{sc}}. \end{aligned} \tag{41}$$

Note that in (40) and (41), the factors composed of trigonometric functions do not vanish on any of the fractures.

The initial and boundary conditions were defined to correspond to the above analytical solution, where we prescribed the Neumann boundary conditions everywhere on $\partial\Omega_{\mathrm{fr}}$ and for $z = -3200.0$ m and $z = -3800.0$ m on $\partial\Omega_{\mathrm{la}}$. On the rest of $\partial\Omega_{\mathrm{la}} \setminus \overline{\Omega_{\mathrm{fr}}}$, we prescribed the Dirichlet boundary conditions.

Thanks to the alignment of the wells, the time-dependent parts of (40) and (41) are zero along the line segments $\boldsymbol{l}_w$ (see Figure 2). Hence, if we consider $(\rho c_p T)|_w(t)$ in (23) and $\Delta p|_w(t)$ in (24) to be functions evaluated along $\boldsymbol{l}_w$, we can compute the quantities in (22)–(24) analytically as well to get $E_{\mathsf{prod}}(t) = 9453461.69$ J/s and $E_{\mathsf{pump}}(t) = 0$ J/s for all t, and $\mathcal{P} = 9453461.69$ W.

We solved the above system numerically using a spatial mesh that was successively refined by uniform splitting 3 times, yielding 4 refinement levels 0, 1, 2, and 3, where the coarsest mesh (level 0) for Ω_{fr} is shown in Figure 4. The numbers of tetrahedra in these meshes were 2091, 16728, 133824, and 1070592. For a level i, we used the time step $\Delta t_i = 0.1 \cdot (t_{\mathrm{fin}} - t_{\mathrm{ini}}) \cdot 4^{-i}$ s, numbers of segments (used in Section 3.2) $N_{w,\mathrm{la}} = 2 \cdot 2^i$ (all segments having the same size) and $N_{w,\mathrm{fr}} = 1$, numbers of points $N_{p,i} = 4 \cdot 2^i$ (used in Section 4.2), and artificial well radii $r_{\varepsilon,i} = r_w + 6.93 \cdot 2^{-i}$ m (that is, when refining the mesh, the difference between r_w and r_ε is halved). Note that the definitions of the above additional sources S_{M} and S_{E} depend on r_ε. This means that the balance equations corresponding to different refinement levels are not exactly the same. One time step for the levels $0, \ldots, 3$ took our numerical solver for the balance equations roughly 0.1 s, 0.5 s, 3.5 s, and 28 s, respectively.

The resulting errors in p, T, $E_{\mathsf{prod}}(t_{\mathrm{fin}})$, $E_{\mathsf{pump}}(t_{\mathrm{fin}})$, and $\mathcal{P}$ are summarized in Tables 2–4. They clearly indicate convergence at least of the first order, the convergence in $\mathcal{P}$ being the fastest.

5.2 Test of solver for optimization problem

We tested the numerical solver for the optimization problem using a setup with realistic values of physical parameters that is simplified enough for us to assess the plausibility of the results.

We considered $\Omega_{\mathrm{la}} = [0.0, 5200.0] \times [0.0, 4350.0] \times [-3350.0, -2450.0]$. There were 41 rectangular fractures inside, 40 of them being parallel and aligned in a column as depicted in Figure 5. The vertices of each

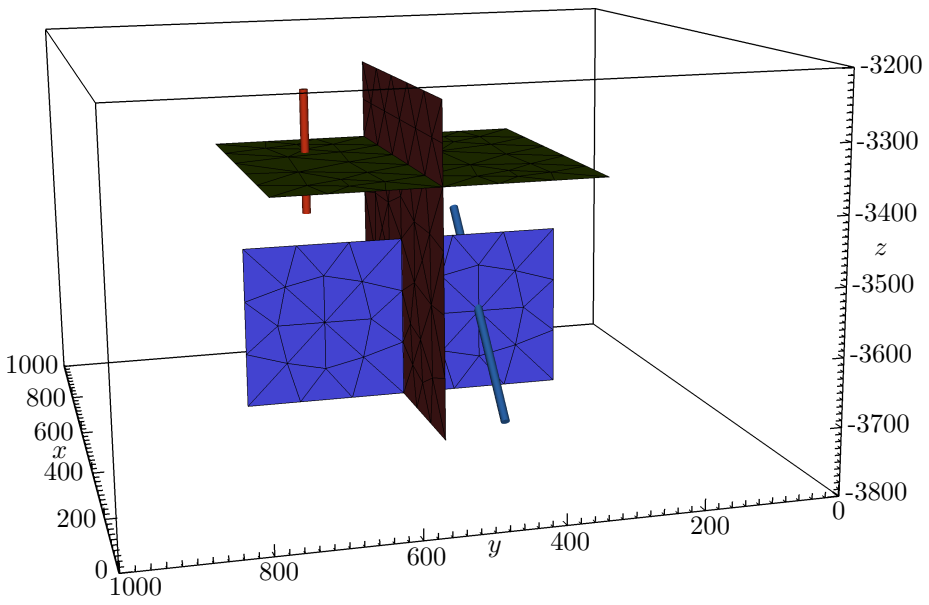

Figure 4: Outline of the domains $\Omega_{\mathrm{la}} = [0, 1000] \times [0, 1000] \times [-3800, -3200]$ and Ω_{fr} used in the convergence test. The fractures are the rectangles $[250, 750] \times [250, 750] \times \{-3375\}$ (green), $[250, 750] \times \{500\} \times [-3250, -3750]$ (brown), and $\{500\} \times [250, 750] \times [-3500, -3750]$ (blue). Note that the perception of the position of the fractures inside the frame is distorted by the rotation of the whole domain; the spatial coordinates are correct. The colors indicate to which population (1, 2, or 3) the fractures belong (green = 1, brown = 2, blue = 3). The cylinders represent the injection (blue) and production (red) wells. The centers of the upper and lower bases of the wells are, respectively, (641.42, 375.0, -3483.58) and (358.58, 375.0, -3766.42) for the injection well, and (625.0, 625.0, -3275.0) and (625.0, 625.0, -3475.0) for the production well.

Parameters in (1)–(3) and (5)–(7)			Parameters in Sections 3.2 and 3.3		
Parameter	Value	Unit	Parameter	Value	Unit
ε_r	0.1	$-$	ρ_w	983.75	$\mathsf{kg \cdot m^{-3}}$
$\varepsilon_{r,1}$	0.035	$-$	ρ_w	983.75	$\mathsf{kg \cdot m^{-3}}$
$\varepsilon_{r,2}$	0.05	$-$	Q_w	± 0.06	$\mathsf{m^{-3} \cdot s^{-1}}$
$\varepsilon_{r,3}$	0.02	$-$	T_w	333.15	K
μ	$2.23 \cdot 10^{-4}$	$\mathsf{Pa \cdot s}$	$c_{p,w}$	4169.7	$\mathsf{J \cdot kg^{-1} \cdot K^{-1}}$
$\boldsymbol{k}$	$3.0 \cdot 10^{-14}$	$\mathsf{m^2}$	r_w	0.07	m
$\boldsymbol{k}_1$	$1.3 \cdot 10^{-10}$	$\mathsf{m^2}$	C_{pen}	10^3	$-$
$\boldsymbol{k}_2$	$5.21 \cdot 10^{-10}$	$\mathsf{m^2}$	ε_w	0.6	$-$
$\boldsymbol{k}_3$	$2.08 \cdot 10^{-11}$	$\mathsf{m^2}$			
g	-9.81	$\mathsf{m \cdot s^{-2}}$	Parameters in Section 5.1		
ρ_r	2730.0	$\mathsf{kg \cdot m^{-3}}$	Parameter	Value	Unit
c_r	2230.0	$\mathsf{J \cdot kg^{-1} \cdot K^{-1}}$	l_{sc}	10^3	m
c_p	4169.7	$\mathsf{J \cdot kg^{-1} \cdot K^{-1}}$	p_{mult}	$2.0 \cdot 10^6$	Pa
λ_r	4.07	$\mathsf{W \cdot m^{-1} \cdot K^{-1}}$	p_{shift}	$30.94 \cdot 10^6$	Pa
λ	0.71	$\mathsf{W \cdot m^{-1} \cdot K^{-1}}$	p_{grad}	$9.3 \cdot 10^6$	$\mathsf{Pa \cdot m^{-1}}$
$d_{\mathrm{fr},1}$	$5.0 \cdot 10^{-5}$	m	T_{mult}	50.0	K
$d_{\mathrm{fr},2}$	$1.0 \cdot 10^{-4}$	m	T_{shift}	379.15	K
$d_{\mathrm{fr},3}$	$2.0 \cdot 10^{-5}$	m	T_{grad}	0.03	$\mathsf{K \cdot m^{-1}}$

Table 1: Values of those constant physical parameters that were the same for all refinement levels. They were defined based on real DFN parameters [27, 21, 33, 28, 23]. The parameters ε_r, $\boldsymbol{k}$, and d_{fr} were fracture-population-specific, where the population number is indicated in the subscript. The values $\boldsymbol{k}_i$ were computed from $d_{\mathrm{fr,i}}$ via the cubic law. The values of μ, c_p, and λ correspond to those of water at 130°C[19]. ρ_w is the density given by (39) at T_w. T_{grad} represents a normal geothermal temperature gradient in the ground, and T_{shift} is the corresponding temperature at a depth of -3.2 km. p_{shift} and p_{grad} represent, respectively, the hydrostatic pressure at a depth of -3.2 km and the average hydrostatic pressure gradient in the reservoir, both corresponding to (39) and the above temperature distribution. Q_w is a typical well flow rate, and ε_w is a typical pump efficiency.

	Error in			
	l_2		l_∞	
level	p in Ω_{la}	p in Ω_{fr}	p in Ω_{la}	p in Ω_{fr}
0	$2.87 \cdot 10^{13}$	$8.53 \cdot 10^{11}$	$2.77 \cdot 10^5$	$2.61 \cdot 10^5$
1	$1.26 \cdot 10^{13}$	$2.91 \cdot 10^{11}$	$1.22 \cdot 10^5$	$8.93 \cdot 10^4$
2	$4.53 \cdot 10^{12}$	$9.10 \cdot 10^{10}$	$4.38 \cdot 10^4$	$2.79 \cdot 10^4$
3	$1.45 \cdot 10^{12}$	$3.00 \cdot 10^{10}$	$1.40 \cdot 10^4$	$9.18 \cdot 10^3$

Table 2: Errors in p for considered mesh refinement levels measured either in l_∞-norm both in time and space or in l_2-norm both in time and space. The time step for these measurements was always $(t_{\mathrm{fin}} - t_{\mathrm{ini}})/10$ s.

	Error in			
	l_2		l_∞	
level	T in Ω_{la}	T in Ω_{fr}	T in Ω_{la}	T in Ω_{fr}
0	$8.20 \cdot 10^8$	$2.92 \cdot 10^7$	$8.58 \cdot 10^0$	$1.03 \cdot 10^1$
1	$3.77 \cdot 10^8$	$9.00 \cdot 10^6$	$3.99 \cdot 10^0$	$3.20 \cdot 10^0$
2	$1.39 \cdot 10^8$	$2.90 \cdot 10^6$	$1.48 \cdot 10^0$	$9.78 \cdot 10^{-1}$
3	$4.81 \cdot 10^7$	$1.17 \cdot 10^6$	$5.46 \cdot 10^{-1}$	$3.41 \cdot 10^{-1}$

Table 3: Errors in T for considered mesh refinement levels measured either in l_∞-norm both in time and space or in l_2-norm both in time and space. The time step for these measurements was always $(t_{\mathrm{fin}} - t_{\mathrm{ini}})/10$ s.

	Error in		
level	$E_{\mathsf{prod}}(t_{\mathrm{fin}})$	$E_{\mathsf{pump}}(t_{\mathrm{fin}})$	$\mathcal{P}$
0	$1.21 \cdot 10^5$	$1.19 \cdot 10^4$	$4.84 \cdot 10^5$
1	$1.09 \cdot 10^5$	$7.76 \cdot 10^3$	$6.41 \cdot 10^4$
2	$4.06 \cdot 10^4$	$2.57 \cdot 10^3$	$8.83 \cdot 10^3$
3	$1.79 \cdot 10^4$	$1.12 \cdot 10^3$	$1.91 \cdot 10^3$

Table 4: Errors in $E_{\mathsf{prod}}(t_{\mathrm{fin}})$, $E_{\mathsf{pump}}(t_{\mathrm{fin}})$, and $\mathcal{P}$ for considered mesh refinement levels.

fracture in the column were

$$(1979.26,\, 2000.0,\, -3067.65 + 10i), \quad (1979.26,\, 2350.0,\, -3067.65 + 10i),$$
$$(2220.74,\, 2350.0,\, -3132.35 + 10i), \quad (2220.74,\, 2000.0,\, -3132.35 + 10i) \quad \text{for } i = 0,\, 1,\, 2, \ldots, 39.$$

The last fracture had vertices

$$(3220.74,\, 2000.0,\, -2867.65), \quad (3220.74,\, 2350.0,\, -2867.65),$$
$$(2979.26,\, 2350.0,\, -2932.35), \quad (2979.26,\, 2000.0,\, -2932.35).$$

There was one couple of vertical wells depicted in Figure 5 inside the domain. The first well, w_1, had the center of the top (3100.0, 2175.0, -2895.0), i.e., 5 m above the last fracture center, and length 10 m. The second well, w_2, went through the above column of fractures, intersecting each fracture in its center, and the vertical coordinate of its top, denoted by z, and length l were used as the optimization parameters. The center of its top was $\boldsymbol{C}_{\mathrm{up}} = (2100.0,\, 2175.0,\, z)$ for $z \in [-3095.0,\, -2705.0]$, and its length was $l \in [10.0,\, 3105.0 + z]$. That is, $\boldsymbol{C}_{\mathrm{up}}$ lay on the line going through the centers of the fractures, and its vertical position ranged from 5 m above the uppermost fracture to 5 m above the lowermost fracture.

The system was simulated for $t_{\mathrm{ini}} = 0$ s and $t_{\mathrm{fin}} = 60 \cdot 60 \cdot 24 \cdot 365 \cdot 50$ s ≈ 50 years, and the constant material properties and parameters had the same values as in Section 5.1, see Table 1, where all fractures belonged to population 2. To reduce the computational costs, the water density was constant, $\rho = 954.20\,\mathrm{kg/m^3}$, which made p and $\boldsymbol{v}$ time-independent.

The initial conditions were

$$p_{\mathrm{ini}}(x, y, z) = 101325.0 - \rho g z, \;\; T_{\mathrm{ini}}(x, y, z) = 283.15 - 0.03z. \tag{42}$$

We prescribed the homogeneous Neumann boundary conditions everywhere on $\partial\Omega_{\mathrm{fr}}$ and for $z = -3350.0$ m and $z = -2450.0$ m on $\partial\Omega_{\mathrm{la}}$. On the rest of $\partial\Omega_{\mathrm{la}} \setminus \overline{\Omega_{\mathrm{fr}}}$, we prescribed the Dirichlet boundary conditions.

The domains were covered by 3 spatial meshes (denoted as *refinement levels 0*, *1*, and *2*): the original mesh and its two successive refinements. The numbers of tetrahedra in these meshes were 170357, 446870, and 3190032, respectively. The original mesh in Ω_{fr} is depicted in Figure 5.

We used this setup to carry out the studies described in the next two sections.

Figure 5: Alignment of the fractures and positions of the first well, w_1 (blue, on the right-hand side) and second well, w_2 (red). The olive-colored lines indicate the coarsest mesh.

5.2.1 Sensitivity study

We tested the dependence of the resulting power $\mathcal{P}$ on the fineness of the spatial mesh, artificial well radius r_ε, exact position of the well, and time step Δt. Employing the above setup, we performed an artificial optimization consisting of the following 720 steps with prescribed settings of wells (i being the step number):

1 $i = 1, \dots, 40$: We consider $w_1 \in \mathcal{W}_{\mathrm{inj}}$ and $w_2 \in \mathcal{W}_{\mathrm{pro}}$. The well w_2 has $z = -2705.0\,\mathrm{m}$ and $l = 10i\,\mathrm{m}$. This means that w_2 has its top fixed $5\,\mathrm{m}$ above the column of fractures and lengthens, crossing i fractures.

2 $i = 41, \dots, 80$: Same as in item 1 but with $z = -3095.0\,\mathrm{m}$ and $l = 10(81 - i)\,\mathrm{m}$. That is, w_2 has its bottom fixed $5\,\mathrm{m}$ below the column of fractures and shortens, crossing $(81 - i) \in [1, 40]$ fractures.

3 $i = 81, \dots, 120$: Same as in item 1 but with $z = -2705.0 - 10(i - 81)\,\mathrm{m}$ and $l = 10\,\mathrm{m}$. That is, when increasing i, we put w_2 deeper, letting it cross only one fracture.

4 $i = 121, \dots, 240$: We perform the same as in items 1–3 but with $\boldsymbol{C}_{\mathrm{up}} = (2100.0,\ 2175.0 + 1.0,\ z)$. That is, we test how the previous results change when shifting the well by $1\,\mathrm{m}$. Therefore, we have $i_{\text{(in items 1–3)}} = i_{\text{(in item 4)}} - 120$.

5 $i = 241, \dots, 360$: We conduct the same as in item 4 but with $\boldsymbol{C}_{\mathrm{up}} = (2100.0,\ 2175.0 + 10.0,\ z)$. That is, we shift the well even farther. It holds $i_{\text{(in items 1–3)}} = i_{\text{(in item 5)}} - 240$.

6 $i = 361, \dots, 720$: We carry out the same as in items 1–5 but with the well types swapped, that is, $w_1 \in \mathcal{W}_{\mathrm{pro}}$ and $w_2 \in \mathcal{W}_{\mathrm{inj}}$. Hence, $i_{\text{(in items 1–5)}} = i_{\text{(in item 6)}} - 360$.

We carried out the above artificial optimization for the time step $\Delta t_3 = (t_{\mathrm{fin}} - t_{\mathrm{ini}})/50$ and all combinations of 3 mesh refinement levels and artificial radii $r_\varepsilon \in \{3.5,\ 7,\ 14\}$. For the refinement level 0 and $r_\varepsilon = 7\,\mathrm{m}$, we also tested the time steps $\Delta t_1 = \Delta t_3/4$, $\Delta t_2 = \Delta t_3/2$, $\Delta t_4 = 2\Delta t_3$, and $\Delta t_5 = 5\Delta t_3$. For the time step Δt_3 and all values of r_ε, one solution of the balance equations on $[t_{\mathrm{ini}}, t_{\mathrm{fin}}]$ took our numerical solver roughly $43\,\mathrm{s}$, $106\,\mathrm{s}$, and $790\,\mathrm{s}$ for the refinement levels 0, 1 and 2, respectively.

The results are depicted in Figures 6–8: Figure 6 confirms that the pressure differences in (24) behave as expected: During steps 1–120, $\left|\ \Delta p|_{w_1}\ \right|$ remains approximately constant, and $\left|\ \Delta p|_{w_2}\ \right|$ is inversely proportional to the number of fractures intersecting w_2. The oscillations in steps 81–120, during which w_2 crossed only 1 fracture, are most probably just due to the non-uniformity of the spatial mesh. Although these oscillations are even around 2 MPa in some cases, their influence on the resulting maximum $\mathcal{P}$ is small because E_{pump} is at least by one order of magnitude smaller than the maxima of E_{prod} for realistic parameter values (see Figure 7, steps 81–120, where the increase in $\mathcal{P}$ is mostly monotone). We can also see that the magnitude of these

oscillations decreases when increasing r_ε or refining the spatial mesh. Shifting w_2 by $1\,\mathrm{m}$ or $10\,\mathrm{m}$ (steps 121–240 and 241–360) seems not to significantly change the results, although it can increase the magnitude of the oscillations for small r_ε on coarse meshes. Switching the well types (steps 361–720) yields results very similar to those for steps 1–360.

Due to the temperature gradient prescribed by (42), the production temperature $T|_{w_2}$ is an increasing function of the step i for $i \in [1,\, 40) \cup [41,\, 80) \cup [81,\, 120) \cup \ldots \cup [321,\, 360)$. Since E_{prod} is an increasing function of $T|_{w_2}$ too, and as mentioned above, E_{pump} is usually much smaller than E_{prod}, we expect $\mathcal{P}$ to increase on the above mentioned intervals for i as well. Figure 7 shows that this is indeed the case, except for approximately the intervals $[76,\, 80)$, $[196,\, 200)$ and $[316,\, 320)$ in the case of small r_ε and refined mesh for which the increase in $\left|\, \Delta p|_{w_2} \,\right|$ is large enough for its effect on $\mathcal{P}$ to be comparable to that of the increased $T|_{w_2}$ (see Figure 6).

In steps 361–720, the length and position of the production well, w_1, were fixed (which kept $T|_{w_1}$ and $\left|\, \Delta p|_{w_1} \,\right|$ approximately constant), and $\mathcal{P}$ should depend mainly on $\left|\, \Delta p|_{w_2} \,\right|$, increasing with decreasing $\left|\, \Delta p|_{w_2} \,\right|$. Figures 6 and 7 clearly show this behavior.

Figure 7 also indicates that $\mathcal{P}$ generally decreases when decreasing r_ε or refining the mesh. The results for the refinement level 0 and $r_\varepsilon = 3.5\,\mathrm{m}$ seem to contradict this tendency, but in this case, r_ε was almost 3 times smaller than the smallest 2D cell diameter, resulting in at least 3 times less cells covering the well-fracture intersections than in all other cases. Consequently, we consider the approximation of the wells in this case poor, and we expect the result to be inaccurate.

Figure 8 indicates that the resulting $\mathcal{P}$ increases when making the time step smaller.

To summarize, the power $\mathcal{P}$ seems to decrease when refining the spatial mesh, making the artificial radius r_ε smaller, or making the time step Δt larger. However, larger values of r_ε appear to make the numerical scheme more robust. Moreover, the results do not seem to be sensitive to small changes in the positions of the wells. The difference in the maximum $\mathcal{P}$ between all the considered setups is up to 6%, which we consider sufficiently small for the intended application.

5.2.2 Optimization study

We tested our framework in a real optimization in which we considered $w_1 \in \mathcal{W}_{\mathrm{inj}}$ and $w_2 \in \mathcal{W}_{\mathrm{pro}}$. To simplify the constraints on the optimization parameters, the set of admissible couples $(z,\, l)$ was bijectively mapped to a unit square in coordinates u and v, where $(z,\, l) = (-3095 + 390u,\, 10 + 390uv)$ for $u, v \in [0,\, 1]$, and these variables u and v were used as the optimization parameters for the algorithms DIRECT and AGS. The simulations were performed for the refinement level 1, $r_\varepsilon = 7\,\mathrm{m}$, and $\Delta t = (t_{\mathrm{fin}} - t_{\mathrm{ini}})/50$.

Moreover, we considered the following two situations:

1 We employed exactly the setup described at the beginning of Section 5.2. In view of the results displayed in Figure 7, we expect the maximum of $\mathcal{P}$ to be attained for w_2 of a length and position similar to the one in step 78 in Section 5.2.1. That is, w_2 should intersect only a few lowermost fractures.

2 We modified the above setup by setting $T_{\mathrm{ini}}(x, y, z) = 400\,\mathrm{K}$ for all $(x, y, z) \in \Omega_{\mathrm{la}}$. Because of the absence of the temperature gradient, we expect $\mathcal{P}$ to be the highest for the smallest $\left|\, \Delta p|_{w_1} \,\right| + \left|\, \Delta p|_{w_2} \,\right|$, that is, for the largest number of fractures intersecting w_2. According to Figure 6, this corresponds to the length and position of the well similar to the one in steps 40 and 41, which describe the same scenario, in Section 5.2.1.

The results displayed in Figures 9–11 confirm our predictions: Figure 9 shows that the optimization algorithms concentrated mainly on searching the parts of the parametric space in which we expect the optimal point to lie. Figures 10 and 11 display the progress of the optimizations. In case 1, both algorithms found solutions that were even better than the one corresponding to step 78 in Section 5.2.1. In case 2, both algorithms found approximately the same solution.

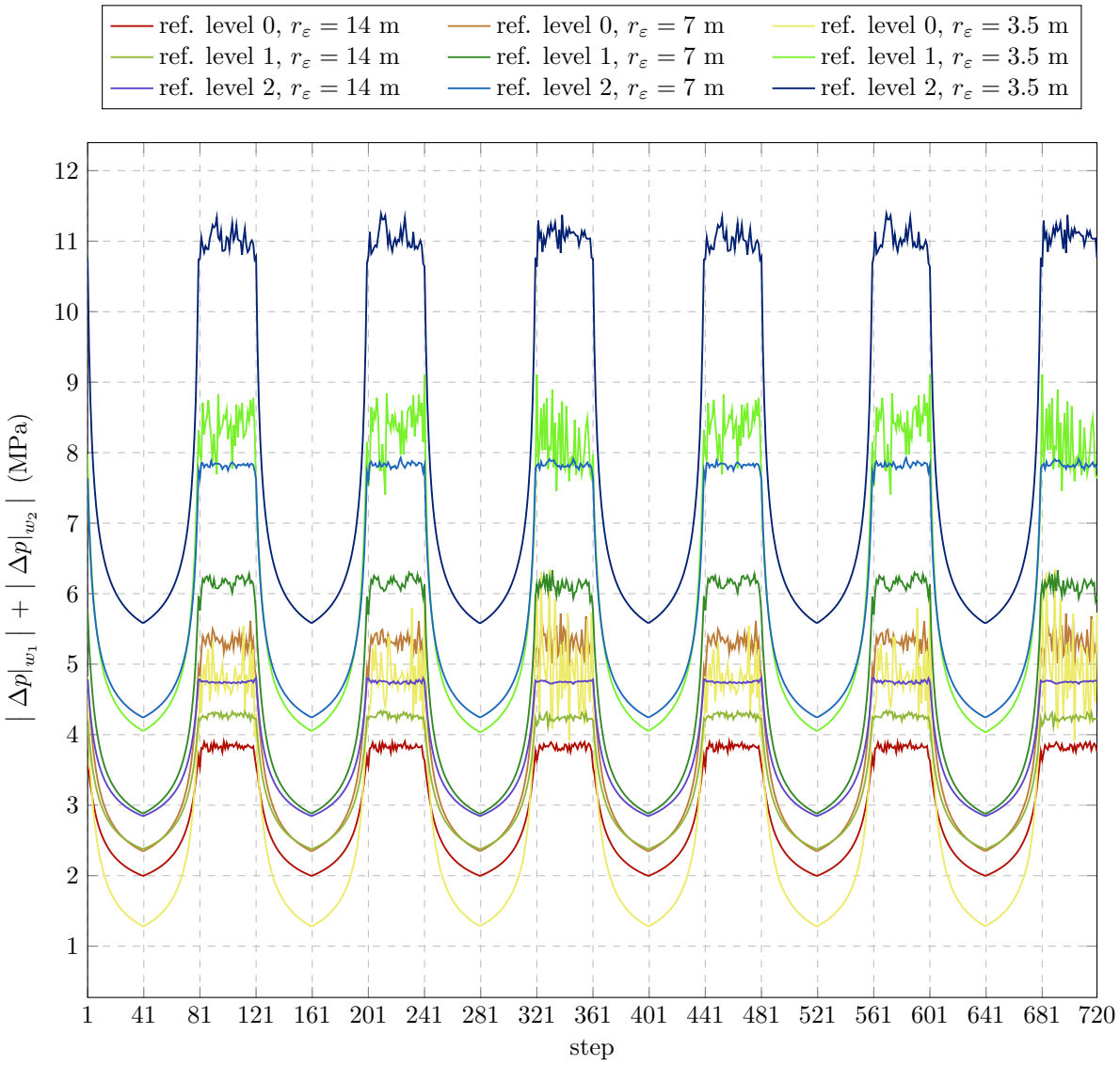

Figure 6: Sum of pressure differences, $\left|\Delta p|_{w_1}\right| + \left|\Delta p|_{w_2}\right|$, in the sensitivity study. In steps 1–360, we had $w_1 \in \mathcal{W}_{\mathrm{inj}}$ and $w_2 \in \mathcal{W}_{\mathrm{pro}}$. In steps 361–720, the well types were swapped.

6 Conclusions

We introduced an efficient numerical framework that enables us to find placements of deviated multiwell layouts (smart multiwell arrangements) in fracture-controlled reservoirs that optimize geothermal energy production. We designed our numerical scheme with a view to creating a fast numerical solver because one solution of the balance equations on $[t_{\mathrm{ini}}, t_{\mathrm{fin}}]$ represents merely one evaluation of the power $\mathcal{P}$ in the process of solving the problem of maximizing $\mathcal{P}$.

We tested our framework using scenarios that considered realistic values of physical parameters but were simplified enough for us to assess the plausibility of the results. Our numerical scheme seems to be at least of the first order, and the results of the optimization tests agree with our expectations. As for the estimated error in the resulting $\mathcal{P}$, we consider it tolerable.

The next step of our work is to apply our framework to reservoirs in the form of large geologically consistent randomly generated DFNs.

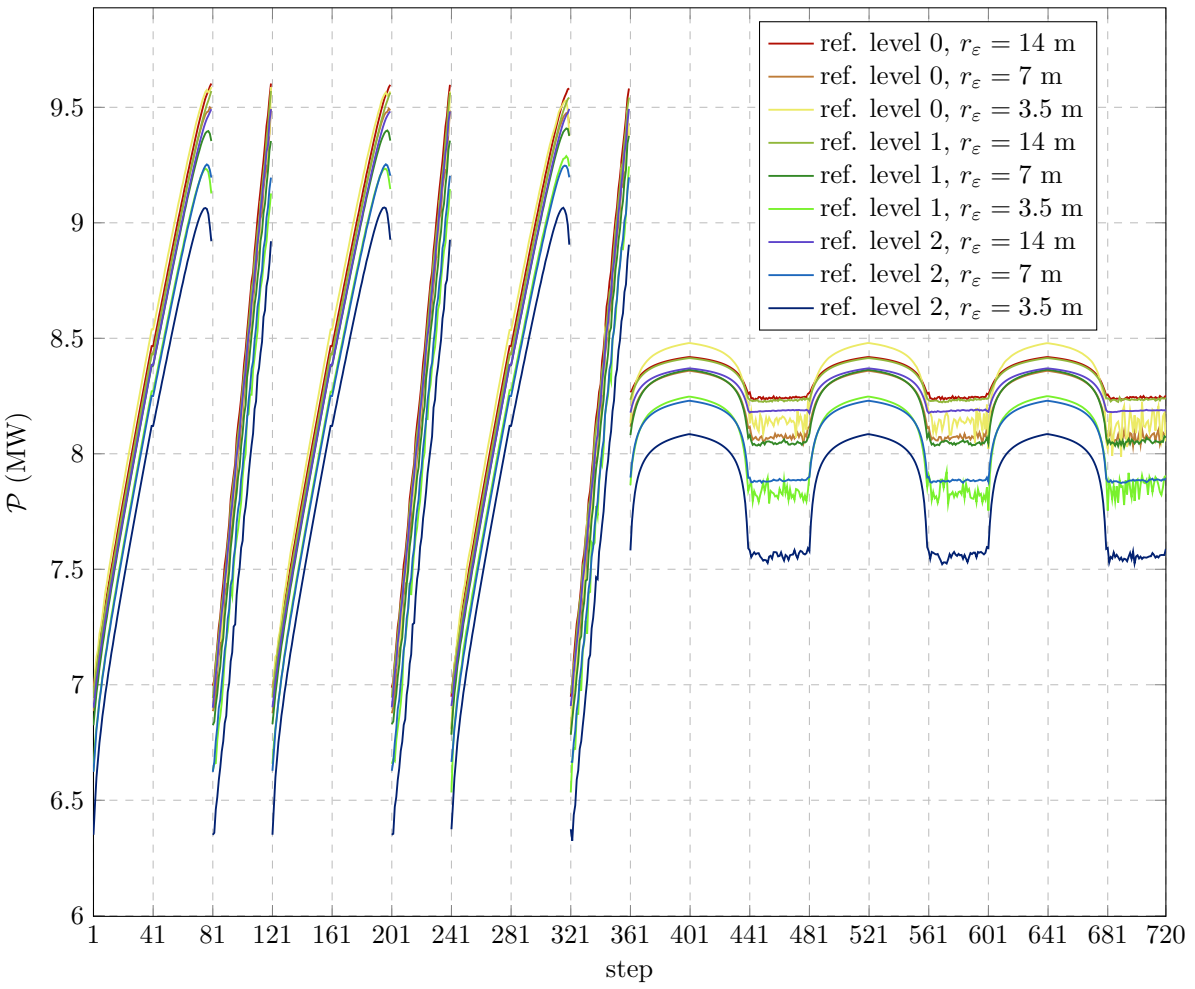

Figure 7: Dependence of the power $\mathcal{P}$ on the artificial radius r_ε and the fineness of the spatial mesh in the sensitivity study. In steps 1–360, we had $w_1 \in \mathcal{W}_{\text{inj}}$ and $w_2 \in \mathcal{W}_{\text{pro}}$. In steps 361–720, the well types were swapped.

References

[1] Pasquale C. Africa, Daniel Arndt, Wolfgang Bangerth, Bruno Blais, Marc Fehling, Rene Gassmöller, Timo Heister, Luca Heltai, Sebastian Kinnewig, Martin Kronbichler, Matthias Maier, Peter Munch, Magdalena Schreter-Fleischhacker, Jan P. Thiele, Bruno Turcksin, David Wells, and Vladimir Yushutin. The deal.II library, version 9.6. *Journal of Numerical Mathematics*, 32(4):369–380, 2024.

[2] Thorsten Agemar, Josef Weber, and Rüdiger Schulz. Deep geothermal energy production in germany. *Energies*, 7(7):4397–4416, 2014.

[3] James Ahrens, Berk Geveci, and Charles Law. ParaView: An end-user tool for large data visualization. *Visualization Handbook*, 2005.

[4] Gabriel R. Barrenechea, Volker John, and Petr Knobloch. Finite element methods respecting the discrete maximum principle for convection-diffusion equations. *SIAM Review*, 66(1):3–88, 2024.

[5] Johannes Birner. *Hydrogeologisches Modell des Malmaquifers im Süddeutschen Molassebecken - Hydrogeological model of the Malm aquifer in the South German Molasse Basin*. PhD thesis, Freie Universität Berlin, Berlin, Germany, jun 2013.

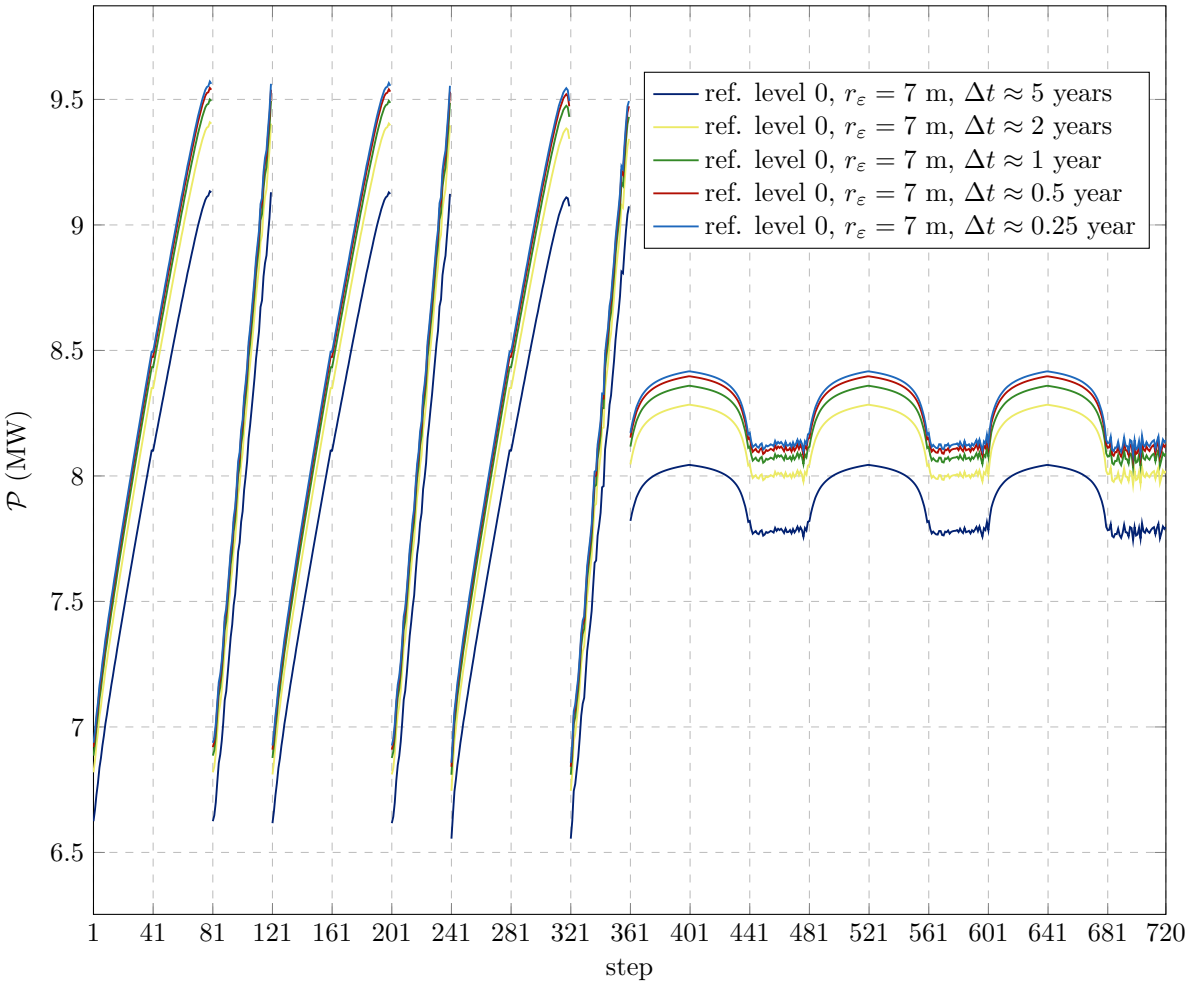

Figure 8: Dependence of the power $\mathcal{P}$ on the time step Δt in the sensitivity study. In steps 1–360, we had $w_1 \in \mathcal{W}_{\text{inj}}$ and $w_2 \in \mathcal{W}_{\text{pro}}$. In steps 361–720, the well types were swapped.

[6] Johannes Birner, Thomas Fritzer, Marco Jodocy, Alexandros Savvatis, Michael Schneider, and Ingrid Stober. Hydraulic characterization of the Malm aquifer in the South German Molasse basin and its impact on geothermal explorations - Hydraulische Eigenschaften des Malmaquifers im Süddeutschen Molassebecken und ihre Bedeutung für die geothermische Erschließung. *Zeitschrift für Geologische Wissenschaften*, 40(2/3):133–156, 12 2012.

[7] Laura Blank, Ernesto Meneses Rioseco, Alfonso Caiazzo, and Ulrich Wilbrandt. Modeling, simulation, and optimization of geothermal energy production from hot sedimentary aquifers. *Computational Geosciences*, 25:67–104, 2021.

[8] Hank Childs, Eric Brugger, Brad Whitlock, Jeremy Meredith, Sean Ahern, David Pugmire, Kathleen Biagas, Mark C. Miller, Cyrus Harrison, Gunther H. Weber, Hari Krishnan, Thomas Fogal, Allen Sanderson, Christoph Garth, E. Wes Bethel, David Camp, Oliver Rubel, Marc Durant, Jean M. Favre, and Paul Navratil. VisIt: An end-user tool for visualizing and analyzing very large data. `https://visit.llnl.gov`, 2012.

[9] M. Dussel, E. Lüschen, R. Thomas, T. Agemar, T. Fritzer, S. Sieblitz, B. Huber, J. Birner, and R. Schulz. Forecast for thermal water use from upper jurassic carbonates in the munich region (south german molasse basin). *Geothermics*, 60:13–30, 2016.

[10] Jocelyne Erhel, Jean-Raynald de Dreuzy, and Baptiste Poirriez. Flow simulation in three-dimensional discrete fracture networks. *SIAM Journal on Scientific Computing*, 31(4):2688–2705, 2009.

[11] Mohamed Fadel, Ernesto Meneses Rioseco, Pierre-Olivier Bruna, and Inga Moeck. Pressure transient analysis to investigate a coupled fracture corridor and a fault damage zone causing an early thermal breakthrough in the north alpine foreland basin. *Geoenergy Science and Engineering*, 229:212072, 2023.

[12] Ingvar B Fridleifsson. Geothermal energy for the benefit of the people. *Renewable and Sustainable Energy Reviews*, 5(3):299–312, 2001.

[13] Christophe Geuzaine and Jean-François Remacle. Gmsh: A 3-D finite element mesh generator with built-in pre- and post-processing facilities. *International Journal for Numerical Methods in Engineering*, 79(11):1309–1331, 2009.

[14] Dennis Gläser, Bernd Flemisch, Holger Class, and Rainer Helmig. Frackit: a framework for stochastic fracture network generation and analysis. *Journal of Open Source Software*, 5:2291, 2020.

[15] Mineyuki Hanano. Contribution of fractures to formation and production of geothermal resources. *Renewable and Sustainable Energy Reviews*, 8(3):223–236, 2004.

[16] Jeffrey D. Hyman, Satish Karra, Nataliia Makedonska, Carl W. Gable, Scott L. Painter, and Hari S. Viswanathan. dfnworks: A discrete fracture network framework for modeling subsurface flow and transport. *Computers & Geosciences*, 84:10–19, 2015.

[17] Abhinav Jha, Ondřej Pártl, Naveed Ahmed, and Dmitri Kuzmin. An assessment of solvers for algebraically stabilized discretizations of convection–diffusion–reaction equations. *Journal of Numerical Mathematics*, 31(2):79–103, 2023.

[18] Steven G. Johnson. The NLopt nonlinear-optimization package. `https://github.com/stevengj/nlopt`, 2007.

[19] Hans-Joachim Kretzschmar and Wolfgang Wagner. *International Steam Tables: Properties of water and steam based on the industrial formulation IAPWS-IF97*. Springer Berlin, Heidelberg, 2014.

[20] Subhash Kumar, Maximilian Loosen, and Reinhard Madlener. Assessing the potential of low-carbon technologies in the german energy system. *Journal of Environmental Management*, 262:110345, 2020.

[21] J.C. Lorenz and S.P. Cooper. *Applied Concepts in Fractured Reservoirs*. John Wiley & Sons Ltd, 2020.

[22] John W Lund and Derek H Freeston. World-wide direct uses of geothermal energy 2000. *Geothermics*, 30(1):29–68, 2001.

[23] Ernesto Meneses Rioseco, Michael Dussel, and Inga S. Moeck. 3D thermo-hydro-mechanical simulation of the behaviour of a naturally fractured petrothermal reservoir in deep upper jurassic carbonates of the bavarian molasse basin – case study geretsried. *Geomechanics and Tunnelling*, 15(1):48–57, 2022.

[24] Inga S. Moeck. Catalog of geothermal play types based on geologic controls. *Renewable and Sustainable Energy Reviews*, 37:867–882, 2014.

[25] Anahi Molar-Cruz, Maximilian F. Keim, Christopher Schifflechner, Markus Loewer, Kai Zosseder, Michael Drews, Christoph Wieland, and Thomas Hamacher. Techno-economic optimization of large-scale deep geothermal district heating systems with long-distance heat transport. *Energy Conversion and Management*, 267:115906, 2022.

[26] Tobias Naegler, Claudia Sutardhio, Anke Weidlich, and Thomas Pregger. Exploring long-term strategies for the german energy transition - a review of multi-sector energy scenarios. *Renewable and Sustainable Energy Transition*, 1:100010, 2021.

[27] Wayne Narr, David S. Schechter, and Laird B. Thompson. *Naturally Fractured Reservoir Characterization*. Society of Petroleum Engineers, 2006.

[28] National Academies of Sciences, Engineering, and Medicine. *Characterization, Modeling, Monitoring, and Remediation of Fractured Rock*. The National Academies Press, 2020.

[29] Adrián E. Ortiz Rojas, Michael Dussel, and Inga Moeck. Borehole geophysical characterisation of a major fault zone in the geothermal Unterhaching gt 2 well, South German Molasse Basin. *Zeitschrift der Deutschen Gesellschaft für Geowissenschaften*, 169(3):445–463, 10 2018.

[30] Jeremy R. Patterson, Michael Cardiff, and Kurt L. Feigl. Optimizing geothermal production in fractured rock reservoirs under uncertainty. *Geothermics*, 88:101906, 2020.

[31] Charles S. Peskin. The immersed boundary method. *Acta Numerica*, 11:479–517, 2002.

[32] Hang Si. TetGen, a delaunay-based quality tetrahedral mesh generator. *ACM Transactions on Mathematical Software*, 41(2), feb 2015.

[33] B.B.S. Singhal and R.P. Gupta. *Applied Concepts in Fractured Reservoirs*. Springer Science+Business Media B.V., 2010.

[34] Joël M. Zinsalo, Louis Lamarche, and Jasmin Raymond. Injection strategies in an enhanced geothermal system based on discrete fractures model. *Applied Thermal Engineering*, 169:114812, 2020.

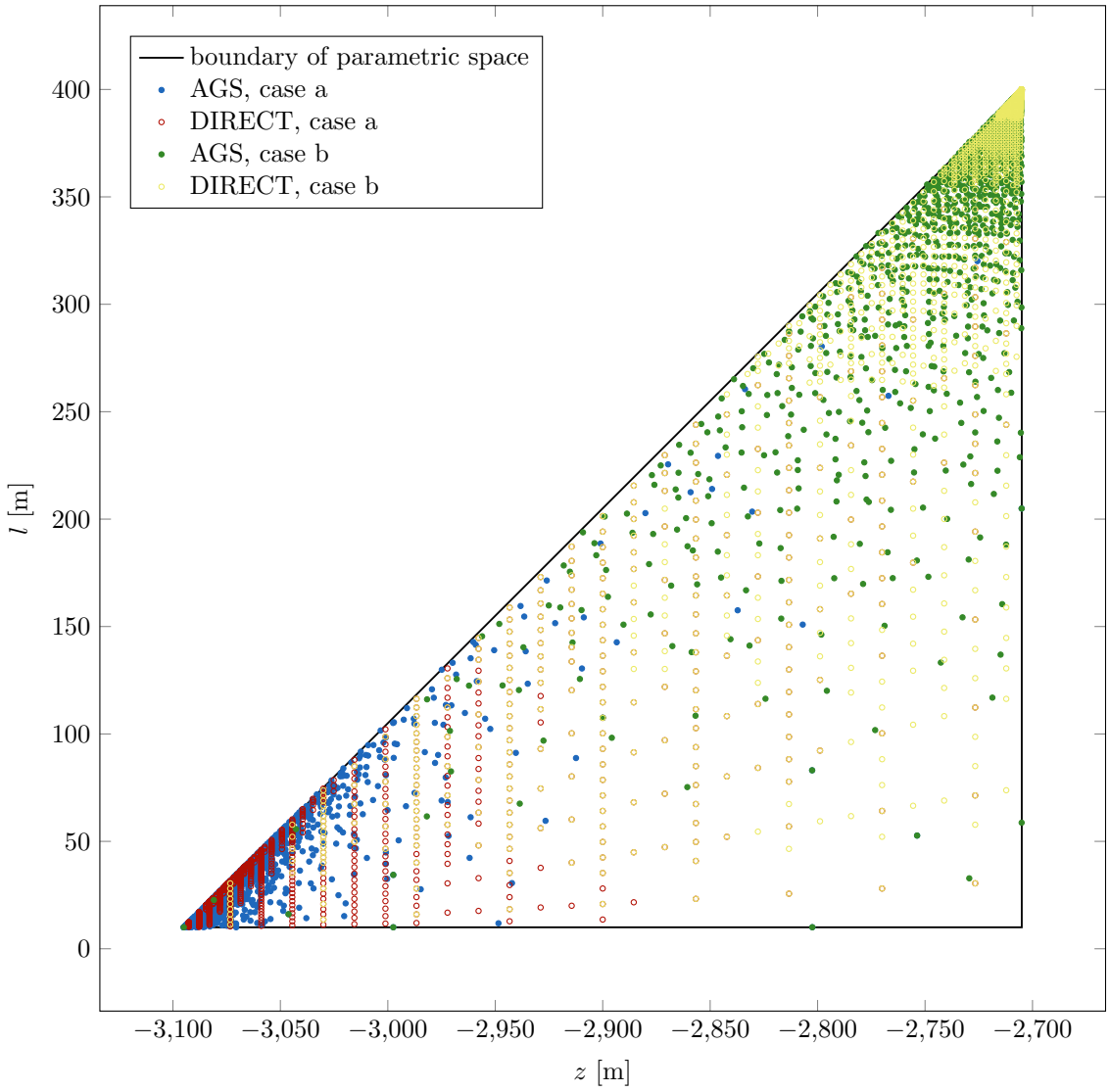

Figure 9: Parametric space of couples $(z,\, l)$, and points indicating the couples tested during the optimization. As expected, in case 1, the concentration of the points is the highest near the point $(-3075,\, 30)$ of the triangle, which represents step 78 in Section 5.2.1. In case 2, the concentration of the points is the highest near the vertex $(-2705,\, 400)$, which corresponds to step 40 in Section 5.2.1.

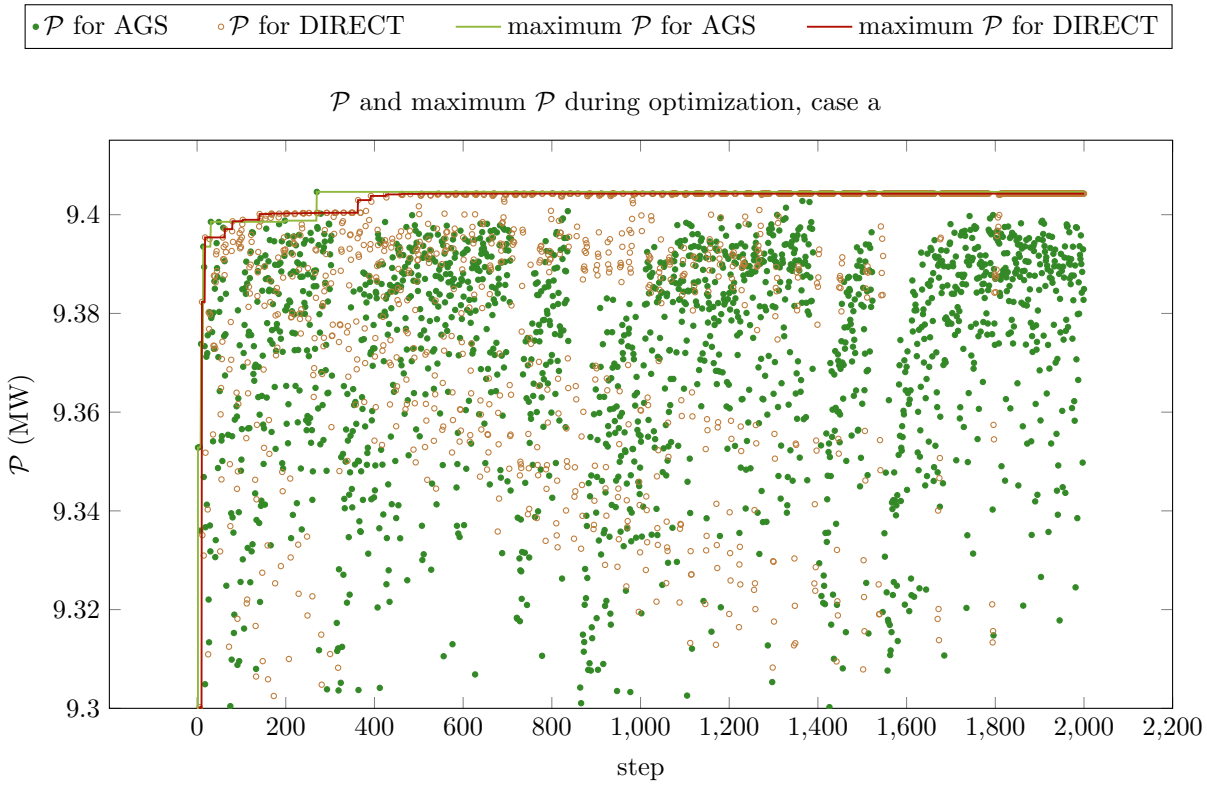

Figure 10: Optimization progress in case 1. Only the part of the graph for $\mathcal{P} \geq 9.3$ MW is displayed, the lowest $\mathcal{P}$ being 7.08 MW. DIRECT found a local maximum 9.4043 MW for $z = -3074.938$ m and $l = 29.979$ m, and the AGS discovered a maximum 9.4046 MW for $z = -3070.958$ m and $l = 33.974$ m. Both algorithms found solution better than the one in step 78 in Section 5.2.1 (which was 9.3972 MW). However, in view of the sensitivity of the numerical scheme indicated by Figures 7 and 8, these differences in $\mathcal{P}$ may be considered negligible.

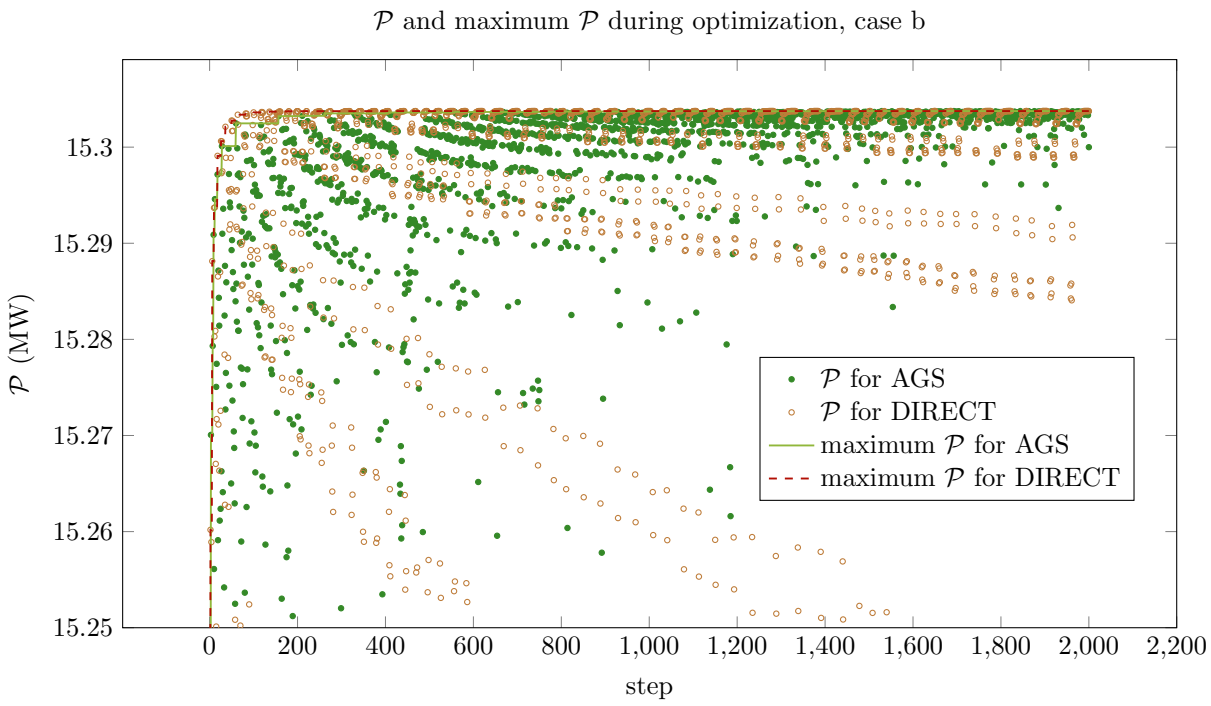

Figure 11: Optimization progress in case 2. Only the part of the graph for $\mathcal{P} \geq 15.25$ MW is displayed, the lowest $\mathcal{P}$ being 14.99 MW. DIRECT found maximum $\mathcal{P} = 15.304$ MW for $z = -2705.046$ m and $l = 399.912$ m. The optimal point for the AGS was $z = -2705.048$ m and $l = 399.905$ m with $\mathcal{P} = 15.304$ MW.